

# Asymmetric Emergence of Low-to-No Snow in the American Cordillera

**Alan Rhoades** (✉ [arhoades@lbl.gov](mailto:arhoades@lbl.gov))

Lawrence Berkeley National Laboratory <https://orcid.org/0000-0003-3723-2422>

**Benjamin Hatchett**

Desert Research Institute

**Mark Risser**

Lawrence Berkeley National Laboratory

**William Collins**

Lawrence Berkeley National Laboratory

**Nicolas Bambach**

University of California, Davis <https://orcid.org/0000-0002-5060-8781>

**Laurie Huning**

California State University, Long Beach <https://orcid.org/0000-0002-0296-4255>

**Rachel McCrary**

**Erica Siirila-Woodburn**

Lawrence Berkeley National Laboratory <https://orcid.org/0000-0001-9406-124X>

**Paul Ullrich**

University of California, Davis

**Michael Wehner**

Lawrence Berkeley National Laboratory <https://orcid.org/0000-0001-5991-0082>

**Colin Zarzycki**

Department of Meteorology and Atmospheric Science, Pennsylvania State University

**Andrew Jones**

Lawrence Berkeley National Laboratory <https://orcid.org/0000-0002-1913-7870>

---

## Article

**Keywords:** snowmelt, low-to-no snow, American Cordillera

**Posted Date:** December 1st, 2021

**DOI:** <https://doi.org/10.21203/rs.3.rs-969310/v1>

**License:** © ⓘ This work is licensed under a Creative Commons Attribution 4.0 International License.

[Read Full License](#)

**Additional Declarations:** There is **NO** Competing Interest.

---

**Version of Record:** A version of this preprint was published at Nature Climate Change on November 14th, 2022. See the published version at <https://doi.org/10.1038/s41558-022-01518-y>.

1 **Asymmetric Emergence of Low-to-No Snow in the**  
2 **American Cordillera**

3 **Alan M. Rhoades<sup>1</sup>, Benjamin J. Hatchett<sup>2</sup>, Mark D. Risser<sup>1</sup>, William D.**  
4 **Collins<sup>1,3</sup>, Nicolas E. Bambach<sup>4</sup>, Laurie S. Huning<sup>5,6</sup>, Rachel McCrary<sup>7</sup>, Erica**  
5 **R. Siirila-Woodburn<sup>8</sup>, Paul A. Ullrich<sup>1,4</sup>, Michael F. Wehner<sup>9</sup>, Colin M.**  
6 **Zarzycki<sup>10</sup>, and Andrew D. Jones<sup>1,11</sup>**

7 <sup>1</sup>Climate and Ecosystem Sciences Division, Lawrence Berkeley National Laboratory, Berkeley, CA, USA

8 <sup>2</sup>Desert Research Institute, Reno, NV, USA

9 <sup>3</sup>Department of Earth and Planetary Science, University of California, Berkeley, CA, USA

10 <sup>4</sup>Department of Land, Air, and Water Resources, University of California, Davis, CA, United States

11 <sup>5</sup>Department of Civil Engineering and Construction Engineering Management, California State University,  
12 Long Beach, CA, USA

13 <sup>6</sup>Department of Civil and Environmental Engineering, University of California, Irvine, CA, USA

14 <sup>7</sup>National Center for Atmospheric Research, Boulder, CO, USA

15 <sup>8</sup>Energy Geosciences Division, Lawrence Berkeley National Laboratory, Berkeley, CA, USA

16 <sup>9</sup>Computational Research Division, Lawrence Berkeley National Laboratory, Berkeley, CA, USA

17 <sup>10</sup>Department of Meteorology and Atmospheric Science, Penn State University, State College, PA, USA

18 <sup>11</sup>Energy and Resources Group, University of California, Berkeley, Berkeley, CA, USA

---

Corresponding author: Alan M. Rhoades, [arhoades@lbl.gov](mailto:arhoades@lbl.gov)

19 **Abstract**

20 Societies and ecosystems within and downstream of mountains rely on seasonal snowmelt  
21 to satisfy their water demands. Anthropogenic climate change has reduced mountain snow-  
22 packs worldwide, altering snowmelt magnitude and timing. Here, the global warming  
23 level leading to widespread and persistent mountain snowpack decline, termed low-to-  
24 no snow, is estimated for the world’s most latitudinally contiguous mountain range, the  
25 American Cordillera. We show a combination of dynamical, thermodynamical, and hyp-  
26 sometric factors results in an asymmetric emergence of low-to-no snow conditions within  
27 the midlatitudes of the American Cordillera. Low-to-no snow emergence occurs approx-  
28 imately 20 years earlier in the Southern Hemisphere, at a third of the local warming level,  
29 and coincides with runoff efficiency declines in both dry and wet years. Prevention of a  
30 low-to-no snow future in either hemisphere requires the level of global warming to be held  
31 to, at most, +2.5 °C.

32 Mountains comprise 12% of the global land area, outside of Antarctica, yet dispro-  
33 portionately influence atmospheric, hydrologic, and cryospheric processes across a con-  
34 tinuum of spatio-temporal scales (Körner et al., 2011). Through the orographic enhance-  
35 ment of precipitation, mountains extract moisture from the atmosphere and store por-  
36 tions of this water in the form of seasonal snow, glaciers, surface water, soil moisture,  
37 and groundwater (Humboldt & Bonpland, 1807; Barry, 1992; Paulsen & Körner, 2014;  
38 Huss et al., 2017; Smith, 2019). As a result, mountain-derived water supports approx-  
39 imately 22% of the world’s water resource needs (Immerzeel et al., 2020).

40 The American Cordillera is the most latitudinally contiguous mountain range in  
41 the world. The land-surface characteristics and hydrologic cycles in the midlatitudes of  
42 the American Cordillera have often been described as “distorted mirror images” of one  
43 another, shaped by comparable storm types (e.g., atmospheric rivers; Payne et al., 2020),  
44 seasonal snowpack dynamics (Huss et al., 2017), and distinct periods of aridity which  
45 give rise to analogous ecosystems (Mooney et al., 1970; di Castri, 1973; Cody & Mooney,  
46 1978; Körner et al., 2011). Societies in these regions monitor the volume of water stored  
47 as snow and the timing of snowmelt to meet water demand in productive agricultural  
48 valleys and populous urban areas.

49 Anthropogenic climate change is expected to fundamentally alter the hydrologic  
50 cycle in mountains (Huss et al., 2017; Immerzeel et al., 2020; Viviroli et al., 2020; Siirila-  
51 Woodburn et al., 2021). These alterations include phase changes in precipitation, decreased  
52 snowpack and glacial storage, and amplified warming with increasing elevation (Pepin  
53 et al., 2015; Sturm et al., 2017; Huss et al., 2017). To date, the combined effect of these  
54 alterations has resulted in unprecedented aridity in the Intermountain West, or the re-  
55 gion encompassing the Cascades and Sierra Nevada through the Rockies, and the Chilean  
56 Andes (Garreaud et al., 2020; Milly & Dunne, 2020; Muñoz et al., 2020; Overpeck & Udall,  
57 2020; Serrano-Notivoli et al., 2021). Coinciding with this enhanced aridity, observations  
58 indicate with high-confidence that mountain snow cover has appreciably declined (Hock  
59 et al., 2019). If trends in model projections continue, deleterious, widespread, and per-  
60 sistent impacts on downstream water resource availability and timing could occur across  
61 the American Cordillera (Sturm et al., 2017; Siirila-Woodburn et al., 2021). This out-  
62 come is referred to as a low-to-no snow future.

63 Although the midlatitudes of the American Cordillera have historically shared com-  
64 mon hydroclimatic characteristics, there is evidence in the paleoclimate and recent his-  
65 torical record that hemispheric changes induced by climate change may be asymmetric  
66 (Held & Soden, 2006; Xu & Ramanathan, 2012; Friedman et al., 2013; Putnam & Broecker,  
67 2017; Allan et al., 2020). This is due to cross-scale interactions at larger scales through  
68 differential alterations to the general circulation and the jet-stream which in turn influ-  
69 ences the midlatitude storm track location, variability, and persistence (Xu & Ramanathan,  
70 2012; Friedman et al., 2013); at regional scales through thermodynamic changes in storm-  
71 type characteristics and land-surface warming (Pepin et al., 2015; Payne et al., 2020);  
72 and at local scales through factors associated with mountain hypsometry such as topo-  
73 graphic height, slope, and ruggedness (Amatulli et al., 2018; Shea et al., 2021).

74 Hemispheric asymmetries in response to anthropogenic climate change also imply  
75 that the emergence of low-to-no snow conditions may occur at different times in, for ex-  
76 ample, the Intermountain West versus the Chilean Andes, as a consequence of cross-scale  
77 interactions between dynamical, thermodynamical and hypsometric factors. Asymme-  
78 tries could arise through alterations in large-scale teleconnections (e.g., the El Niño South-  
79 ern Oscillation; Patricola et al., 2019), the genesis and landfall location of storms (Payne  
80 et al., 2020), the efficiency at which mountains extract moisture from the atmosphere  
81 (Eidhammer et al., 2018), the elevation of the freezing level (Lynn et al., 2020), the snow-

82 fall fraction of storms (Bales et al., 2006), and the evolution of snowpack cold-content  
83 (Jennings et al., 2018) that drives metamorphism and eventual snowmelt (Colombo et  
84 al., 2019). Therefore, it is imperative to understand and estimate how these cross-scale  
85 interactions influence the emergence of a low-to-no snow future across the American Cordillera,  
86 particularly for instilling resilience into water resource management.

## 87 **Identifying Low-to-No Snow Emergence**

88 The inherent challenges in modeling the cross-scale interactions that shape the moun-  
89 tainous hydrologic cycle pose a scientific grand challenge, particularly in estimating the  
90 time horizon, spatial extent, and magnitude of low-to-no snow conditions (Siirila-Woodburn  
91 et al., 2021). Simulating decadal to centennial length changes in mountain hydrology at  
92 global-scales with better fidelity requires high-resolution ( $\leq 0.5^\circ$  horizontal resolution as  
93 discussed by Demory et al., 2013) and cannot be done with traditional Earth system model  
94 simulations (Rhoades et al., 2017; Kapnick et al., 2018; Palazzi et al., 2019). However,  
95 recent climate simulations are approaching the resolutions needed to investigate the emer-  
96 gence of a low-to-no snow future in mountains at both global and regional scales. Be-  
97 cause it is one of the first multi-model ensembles that provide simulations at resolutions  
98 needed to capture global scale mountain snowpack dynamics, we leverage the High Res-  
99 olution Model Intercomparison Project (HighResMIP) ensemble (R. J. Haarsma et al.,  
100 2016). We follow Körner et al. (2017) in defining mountains, particularly the American  
101 Cordillera, and Siirila-Woodburn et al. (2021) in quantitatively characterizing low-to-  
102 no snow emergence. The latter definition is based on annual peak snow water equiva-  
103 lent (SWE) percentiles (see Methods). Next, we assess low-to-no snow persistence, its  
104 connection to warming, and identify if there is hemispheric asymmetry. Last, we detail  
105 how the mountainous hydrologic cycle is fundamentally altered following the emergence  
106 of low-to-no snow through alterations in how water is deposited, stored and transferred  
107 downstream.

108 Over the historical period (1950-2000) inter-annual variability in peak SWE is high  
109 along the American Cordillera, representative of a weak signal-to-noise of snow loss (Fig-  
110 ure 1 and S1). The signal of change refers to the trend in peak SWE decline, whereas  
111 the noise is the interannual variability in peak SWE magnitude. The magnitudes of peak  
112 SWE change are also provided (Figure S2). However, between 2025 and 2050, only por-  
113 tions of the American Cordillera exhibit consistent below-median historical peak SWE

114 percentiles. After 2050, below-median historical peak SWE percentiles are consistently  
115 projected across the American Cordillera, indicating a stronger signal-to-noise emergence  
116 (Figure 1). Notably, this systematic emergence roughly coincides with a divergence in  
117 hemispheric warming and associated differences in mean meridional overturning circu-  
118 lation, indicating differing mechanistic influences on low-to-no snow emergence (Figure  
119 S3). Given the weakening of the Northern Hemisphere general circulation, low-to-no snow  
120 emergence is shaped by both dynamically-induced storm track shifts and thermodynamic  
121 controls on landfalling storm precipitation amount and phase and snowpack ripening due  
122 to warmer temperatures. In the Southern Hemisphere, the general circulation shows lit-  
123 tle response to warming and low-to-no snow emergence is controlled primarily through  
124 thermodynamic controls.

125 While decreases in mean peak SWE for 2015-2050 relative to 1950-2000 are con-  
126 sistent and statistically significant in California’s Sierra Nevada (4/6 simulations), re-  
127 sults are less consistent throughout the Pacific Northwest and North American Rock-  
128 ies (Figure S4). This result is shaped by differential changes in annual mean total pre-  
129 cipitation (Figure S5) and surface air temperature within individual simulations (Fig-  
130 ure S6). In the Southern Hemisphere, models project (4/6 simulations) increases in mean  
131 peak SWE (Figure S7). This results from increases in annual mean total precipitation  
132 (Figure S8) combined with weaker, though significant, annual mean surface air temper-  
133 ature increases compared with the Northern Hemisphere (Figure S9). However, a sig-  
134 nificant decrease in mean peak SWE in both hemispheres is found by the two models  
135 that project out to 2100, save for certain portions of the Canadian Rockies and north-  
136 ern Chilean Andes (Figure S4d,e and S7d,e).

137 Although Figure 1 demonstrates a clear transition from normal snow-conditions  
138 to a future of low-to-no snow, it does not enable precise isolation of the emergence and  
139 persistence of snow loss given the difficulties in identifying a trend signal between 1950-  
140 2050. Hereafter, we focus our analysis on the highest-resolution model simulation (20 km;  
141 MRI-AGCM3-2-S) of the two available 150-year projections (1950-2099) in the HighResMIP  
142 ensemble to investigate the date-of- and degrees-to-emergence of low-to-no snow within  
143 the American Cordillera. To isolate the date at which snowpack depletion begins to ap-  
144 preciably impact the mountainous hydrologic cycle, we define thresholds for low-to-no  
145 snow conditions at three different sequential time periods (see Methods): extreme (back-  
146 to-back low-to-no snow years), episodic (low-to-no snow spanning 5-years), and persis-

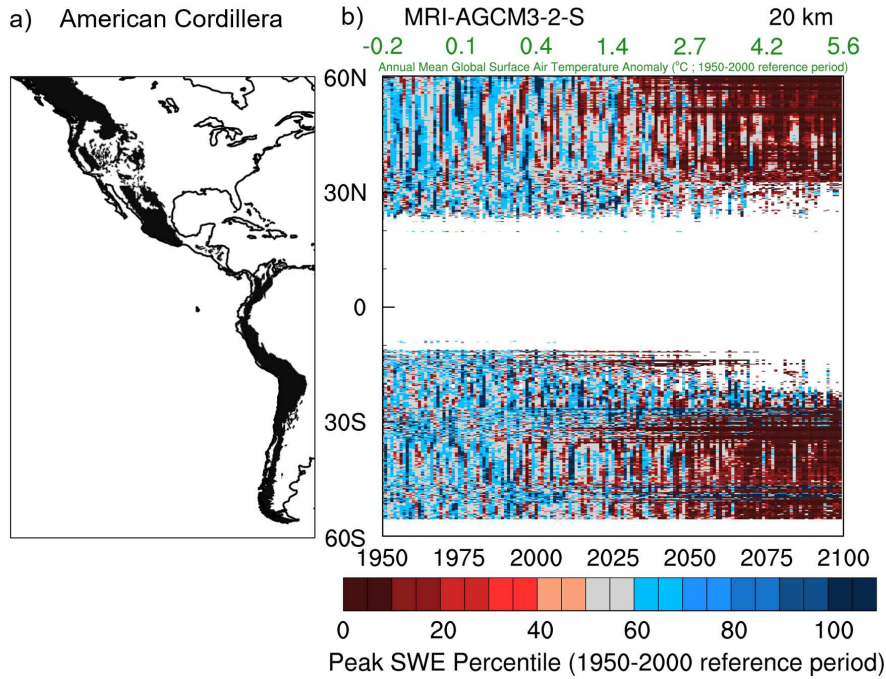


**Figure 1.** a) American Cordillera (black polygon) from 60° N to 60° S. b) latitude band averages of annual peak snow water equivalent (SWE) percentiles within the American Cordillera as simulated by the highest resolution (20 km) HighResMIP simulation (MRI-AGCM3-2-S) over 1950-2100 under the high-emissions shared socioeconomic pathway (SSP585). The top x-axis shows the annual mean global surface air temperature anomalies and the bottom x-axis indicates the dates between 1950-2100. 1950-2000 is used as the historical reference period to compute percentile bins and annual mean temperature anomalies. White regions indicate annual peak SWE values  $\leq 2.54$  mm or no SWE. Low-to-no snow conditions are defined as latitude-band average annual peak SWE  $\leq 30$ th percentile.

147 tent (low-to-no snow spanning 10-years). To identify hemispheric asymmetry in the emer-  
 148 gence of low-to-no snow we use common latitude bands of  $\pm 32$ - $59^\circ$ . These latitude bands  
 149 are symmetric about one another and comprise mountainous regions that maintain sea-  
 150 sonal snowpacks across the entire 150-year time-period (as indicated by the extensive  
 151 amount of missing values and/or more ephemeral snow conditions between the latitude  
 152 bands of  $\pm 0$ - $32^\circ$  in Figure 1b). The hemispheric-wide emergence of extreme low-to-no  
 153 snow conditions occurs 17 years earlier in the Southern Hemisphere with a median date  
 154 of  $2039_{2015}^{2051}$ , with 95% confidence intervals provided as a superscript and subscript, ver-  
 155 sus  $2056_{2049}^{2062}$  in the Northern Hemisphere (Figure 2a,c). This hemisphere asymmetry in

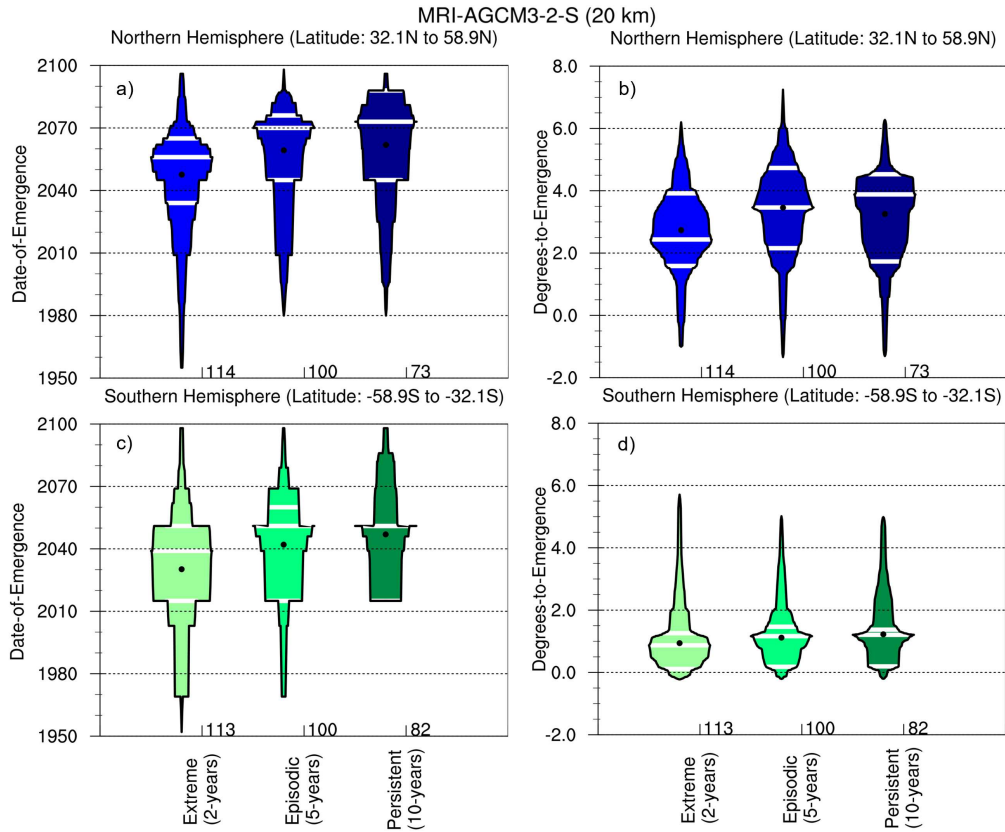


**Figure 2.** Box percentile plots of latitude band average date-of-emergence of low-to-no snow ( $\leq 30$ th percentile historical peak SWE; 1950-2000 historical reference period) for the northern (blue;  $32^{\circ}$  N to  $59^{\circ}$  N) and southern (green;  $32^{\circ}$  S to  $59^{\circ}$  S) midlatitude portions of the American Cordillera. White lines indicate the  $75^{th}$ , median, and  $25^{th}$  percentiles and the black dot represents the mean. The numbers along the x-axis indicate the number of latitude bands that make up the box percentile plot distributions. Date-of-emergence (a, c) is predicated on back-to-back years of low-to-no snow under three conditions, extreme (at least 2-years), episodic (at least 5-years), and persistent (at least 10-years). The degrees-to-emergence (b, d) are local, annual surface air temperature changes from the 1950-2000 reference period at which extreme, episodic and persistent low-to-no snow conditions first occur at a particular latitude band.

156 low-to-no snow emergence timing is approximately the same for the the episodic thresh-  
 157 old (hemispheric difference of 19 years) and persistent threshold (hemispheric difference  
 158 of 22 years). Given the convergence in the median date-of-emergence of low-to-no snow  
 159 conditions between the episodic and persistent thresholds (Figure 2a,c) post-emergence  
 160 of low-to-no snow is hereafter defined as all years following emergence of episodic low-

161 to-no snow or 2051<sup>2051</sup><sub>2046</sub> in the Southern Hemisphere and 2070<sup>2073</sup><sub>2065</sub> in the Northern Hemi-  
162 sphere.

163 The Northern Hemisphere, consistent with Xu and Ramanathan (2012) and Friedman  
164 et al. (2013), warms faster than the Southern Hemisphere (Figure S3a), even within the  
165 American Cordillera (Figure S3b). Low-to-no-snow emergence occurs at a median local  
166 surface air temperature change of  $+3.5^{+4.0}_{+3.4}$  °C relative to 1950-2000; whereas in the South-  
167 ern Hemisphere, this occurs with approximately a third of the local warming,  $+1.2^{+1.2}_{+0.9}$   
168 °C (Figure 2b,d). This is partly explained by the historically warmer local annual sur-  
169 face air temperatures in the mountainous regions of the Southern Hemisphere (median  
170 of 5.7 °C over 1950-2000) relative to the Northern Hemisphere (median of 2.7 °C over  
171 1950-2000). From a global warming perspective, low-to-no snow emergence occurs be-  
172 tween +2.4 °C and +2.9 °C (between 2046-2051) in the Southern Hemisphere and +3.5  
173 °C to +4.1 °C (between 2065-2073) in the Northern Hemisphere. Elevation-dependent  
174 warming is also hemispherically asymmetric. Mean elevation-band warming post-2015  
175 in the Northern Hemisphere was +2.9 °C up to 1000m and +3.5 °C between 2000-3000m.  
176 In the Southern Hemisphere, elevation-band warming of +1.4 °C up to 1000m and +2.3  
177 °C between 2000-3000m. Despite the asymmetric increase in surface air temperature in  
178 the Northern Hemisphere, and inclusion of both continental and maritime mountains within  
179 the American Cordillera relative to the Southern Hemisphere, the net result is symmet-  
180 ric convergence in hemispheric median annual surface air temperatures ( $\sim 7.5$  °C) over  
181 the years post-emergence of low-to-no snow.

## 182 **Post-Emergence Implications of Low-to-No Snow**

183 Although hemispheric symmetry in annual mean surface air temperatures in the  
184 American Cordillera occurs over the years post-emergence of low-to-no snow (Figure 3a)  
185 asymmetric mountain hydrologic cycle responses arise. This reflects shifts in both an-  
186 nual mean total precipitation (Figure 3b) and the fraction of precipitation falling as snow,  
187 or snowfall fraction (Figure 3c). Historically, Southern Hemisphere mountains receive  
188 more than twice as much precipitation (median of 3000 mm) than the Northern Hemi-  
189 sphere (median of 1300 mm). Yet, the change in total precipitation is more consistent  
190 in sign with latitude in the Southern Hemisphere following emergence of low-to-no snow  
191 (median of -9%). Historically, the Southern Hemisphere also receives a smaller fraction  
192 of precipitation as snowfall (median of 12%) than the Northern Hemisphere (median of

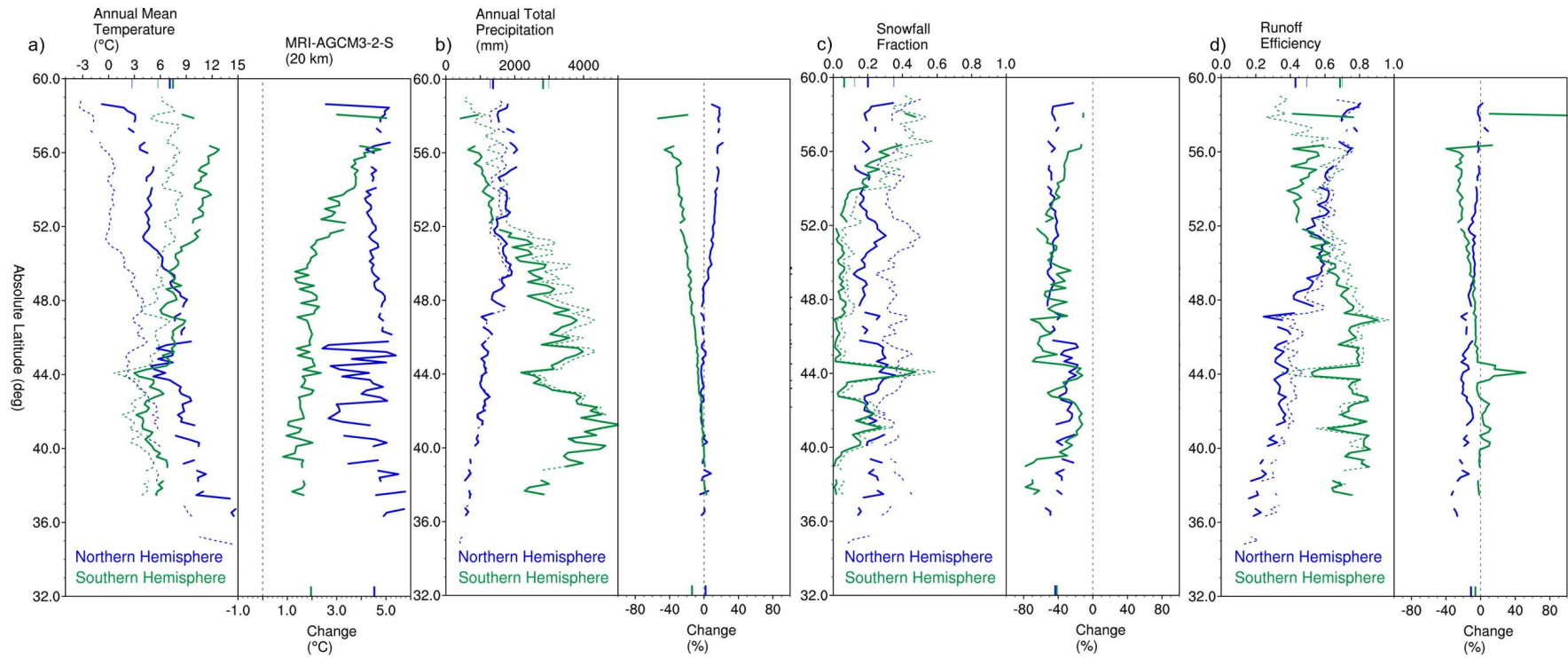


**Figure 3.** Latitude band mean hydrologic cycle responses within the Northern (blue) and Southern (green) midlatitudes of the American Cordillera for all years post-emergence of low-to-no snow. a) annual mean surface air temperature, b) annual mean total precipitation, c) annual mean snowfall fraction (total snowfall/total precipitation) and d) annual mean runoff efficiency (total runoff/total precipitation) and their changes for all years post-emergence of low-to-no snow (right-hand side of each subplot) are shown. Changes are all relative to the 1950-2000 historical reference period. Historical values are shown with dashed lines. Midlatitude wide median values for both historical and post-emergence of low-to-no snow are shown via colored tickmarks along the x-axes. A dotted zero-line is also provided in each subplot showing hydrologic cycle changes post-emergence of low-to-no snow relative to the historical reference period.

193 35%), however the net decline in snowfall fraction is comparable (median of -42%) fol-  
194 lowing emergence of low-to-no snow (Figure 3c). For the Northern Hemisphere the pre-  
195 cipitation that falls on the surface without pre-existing snow cover increases from 45%  
196 to 67% of the total precipitation fraction (Figure S12). In the Southern Hemisphere the  
197 precipitation that falls on the surface without pre-existing snow cover increases by only  
198 10% (73% to 83%), but still remains higher than in the Northern Hemisphere. This co-  
199 incides with a marked decrease in the mean number of freezing days from 137 to 83 and  
200 65 to 34 in the Northern and Southern Hemispheres, respectively. Freezing day shifts re-  
201 sult in changes in the percent of total precipitation that comes as snowfall on pre-existing  
202 snow cover from 43% to 24% in the Northern Hemisphere and from 21% to 14% in the  
203 Southern Hemisphere.

204 The combined effect of warmer surface air temperatures, increased rainfall, and less  
205 snowpack post-emergence of low-to-no snow alters runoff generation in mountains (Fig-  
206 ure S10 and S11). Runoff efficiency relates the amount of total precipitation and total  
207 runoff in a given year (Figure 3d). Temperature strongly dictates changes in runoff ef-  
208 ficiency (Woodhouse & Pederson, 2018) through changes in evaporative demand (Lehner  
209 et al., 2017; Overpeck & Udall, 2020) and seasonal snowpack amounts which acts as a  
210 more efficient and predictable runoff generator than rainfall (Berghuijs et al., 2014; Li  
211 et al., 2017; Livneh & Badger, 2020). In the Northern Hemisphere, a clear monotonic  
212 relationship between latitude and runoff efficiency exists over the historical period (Fig-  
213 ure 3d). This relationship is not as evident in the Southern Hemisphere (Figure 3d). De-  
214 spite the weaker relationship between runoff efficiency and latitude in the Southern Hemi-  
215 sphere there is a more consistent amount of historical runoff efficiency across latitudes  
216 (median of 70% versus 49% in the Northern Hemisphere). This relationship could be due  
217 to differences in mountain slope (higher throughout the Southern Hemisphere) and veg-  
218 etation distributions with elevation (less in the Southern Hemisphere). Post-emergence  
219 of low-to-no snow, the Northern Hemisphere has a consistent decrease in runoff efficiency  
220 (median of -11%), whereas in the Southern Hemisphere a more heterogeneous response  
221 occurs with increases or decreases generally demarcated above or below latitude 44°S,  
222 respectively.

223 Despite increases in runoff efficiency with latitude (Figure 3d and 4a,d), the spa-  
224 tial patterns of historic runoff efficiency also demonstrate the influence of continental-  
225 ity (Figure 4a) in the Northern Hemisphere with coastal mountains yielding higher runoff

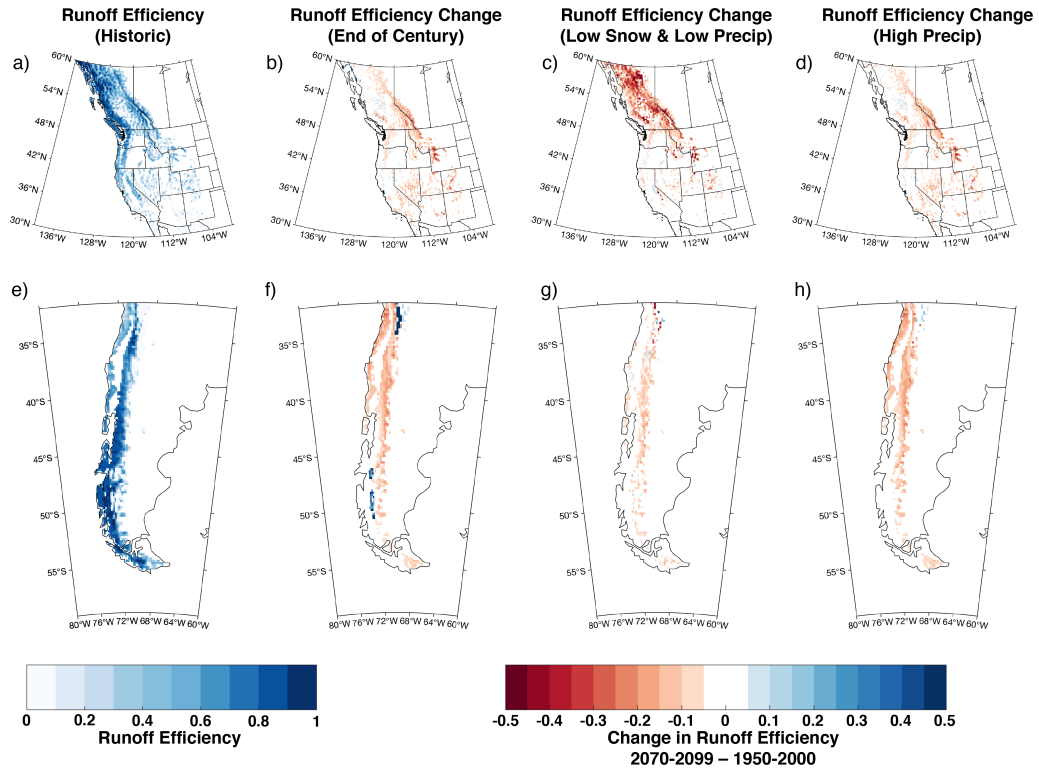


**Figure 4.** Spatial patterns of runoff efficiency for the Northern Hemisphere (30° N to 60° N; top row) and the Southern Hemisphere (32° S to 59° S; bottom row). In the Northern Hemisphere, runoff efficiency (total annual runoff over the total annual precipitation) is determined over October through September of the following year. In the Southern Hemisphere, runoff efficiency is determined from January through December of the same year. a,e) Median annual runoff efficiency. b,f) Change in runoff efficiency for the end of the century compared to the 1950-2000 historical reference period. c,g) As in b,f) but for peak SWE and precipitation  $\leq 30$ th historical reference period percentile. d,h) As in b,f) but for high precipitation years ( $\geq 70$ th historical percentile) when runoff  $\geq 30$ th historical percentile.

226 efficiency. With a few exceptions, mountain regions in both hemispheres are projected  
 227 to undergo declines in runoff efficiency as a result of warming (Figure 4b,f). The largest  
 228 changes are projected for the interior Rocky Mountains (Figure 4b) and the Central Chilean  
 229 Andes (Figure 4e). Exceptions occur in the Coastal Ranges of British Columbia and Patag-  
 230 onia where glacial melt will increase runoff as well as in the northern Chilean Andes where  
 231 extreme precipitation is projected to increase (Bambach et al., 2021). As a result of warm-  
 232 ing and the emergence of low-to-no snow conditions in the late 21st century, we consider

233 two types of years to examine runoff changes: 1) low snow and low precipitation years  
234 and 2) high precipitation years. In the relatively colder historical climate, low snow years  
235 are tied more directly to low precipitation. In the future, precipitation variability and  
236 snowpack variability become more uncoupled. Declines in runoff efficiency during low  
237 snow and low precipitation years are greatest in the northern Rockies (Figure 4c) and  
238 central Chilean Andes (Figure 4g). Runoff efficiency also decreases during future wet years  
239 (Figure 4d,h). This is shaped by an increase in atmospheric demand for water through-  
240 out the year and a future limit on evaporation associated with less snowpack and soil  
241 moisture in drier months (Milly & Dunne, 2020). These results suggest a net reduction  
242 in the capability of American Cordillera mountains to reliably provide water resources  
243 to downstream users post-emergence of low-to-no snow conditions.

## 244 Discussion

245 While the hydrologic cycles in the midlatitudes of the American Cordillera have  
246 historically been “distorted mirror images” of one another, their projected response to  
247 climate change is asymmetric. We found hemispheric asymmetries in the emergence of  
248 low-to-no snow conditions, or when snow loss becomes deleterious, widespread, and per-  
249 sistent. Low-to-no snow emergence is projected to occur in the Northern Hemisphere at  
250  $2070_{2065}^{2073}$  at a local warming level of  $+3.5_{+3.4}^{+4.0}$  °C. However, in the Southern Hemisphere  
251 low-to-no snow emergence is projected to occur at  $2051_{2046}^{2051}$  at a local warming level of  
252  $+1.2_{+0.9}^{+1.2}$  °C. This asymmetry in low-to-no snow emergence is not only a function of hyp-  
253 sometric differences along the American Cordillera, but also changes across spatial scales.  
254 At planetary scales, a shift in the atmospheric general circulation (e.g., meridional slow-  
255 down in the Northern Hemisphere) was found and is related to asymmetric hemispheric  
256 warming. At regional scales, changes brought about by alterations to landfalling storm  
257 characteristics (e.g., heterogeneous changes to annual total precipitation and ubiquitous  
258 reductions in snowfall fraction) and more localized elevation-dependent warming were  
259 identified. Our findings suggest that the prevention of low-to-no snow emergence in ei-  
260 ther hemisphere requires global warming to be limited to, at most, +2.5 °C.

261 In the midlatitudes of the American Cordillera, mountain runoff is critically im-  
262 portant to meeting water demands through replenishment of downstream surface reser-  
263 vairs and by buffering against dry season aridity. Post-emergence of low-to-no snow, an-  
264 nual runoff efficiency markedly declines throughout the American Cordillera. The an-

265 nual runoff declines are of greatest magnitude during future dry years, though even wet  
266 years will see mountains generally become less efficient at generating runoff as loss of snow-  
267 pack enhances evaporative losses (Milly & Dunne, 2020). Decreased water availability  
268 from surface water in both dry and wet years yield two outcomes. First, future dry years  
269 will experience exacerbated drought conditions compared to historic dry years. Second,  
270 less efficient runoff in future wet years implies these years will not ameliorate drought  
271 as effectively as in the historical record. Risks associated with markedly reduced runoff  
272 pose direct challenges to an already complex decision-making system (Huss et al., 2017;  
273 Sturm et al., 2017; Immerzeel et al., 2020; Siirila-Woodburn et al., 2021). These risks  
274 are heightened by centuries of infrastructure design and management strategies that have  
275 largely assumed climate stationarity (Milly et al., 2008; Cosgrove & Loucks, 2015). Fur-  
276 ther compounding these risks, the southern midlatitudes of the American Cordillera are  
277 projected to face low-to-no snow emergence nearly 20 years earlier than the northern mid-  
278 latitudes. This warrants attention and action as the southern Chilean Andes have the  
279 highest global water tower index outside of Asia (Immerzeel et al., 2020), yet the region  
280 has significantly less built infrastructure, monitoring networks, and forecasting centers  
281 that could instill resilience to these hydrologic cycle alterations. The cross-hemispheric  
282 perspective of low-to-no snow emergence also demonstrates shared commonalities across  
283 regions and highlights the need for a pro-active exchange of policy interventions (Castilla-  
284 Rho et al., 2019), cutting-edge water management strategies (Scanlon et al., 2016; Sterle  
285 et al., 2019; Dillon et al., 2019; Delaney et al., 2020) and conceptual frameworks (Szinai  
286 et al., 2020; Vicuña et al., 2021). Most importantly, it highlights the need to implement  
287 carbon mitigation strategies at scale (Williams et al., 2021) that inhibit the global warm-  
288 ing level at which persistent low-to-no snow conditions emerge.

## 289 **Methods**

### 290 **High-Resolution Model Intercomparison Project (HighResMIP v1.0)**

291 To assess American Cordillera hydrologic cycle changes, we leverage the HighResMIP  
292 ensemble (R. J. Haarsma et al., 2016; Roberts et al., 2019, 2020). Participation in High-  
293 ResMIP entailed that modeling centers would provide, at least, one ensemble member  
294 for one of five model experiment Tiers:

- 295 (1) 1950-2050 AMIP-style simulations.

- 296 (2) 1950-2050 fully-coupled simulations (high-emission scenario, SSP585 analogous to  
297 RCP8.5).
- 298 (3) 2051-2100 extension on Tier 1 and/or Tier 2
- 299 (4,5) idealized aquaplanet and abrupt-4xCO<sub>2</sub> perturbations

300 For most of the simulations daily outputs of snow water equivalent (SWE; *snw*),  
301 surface air temperature (*tas*), precipitation (*pr*), snowfall (*prsn*), and runoff (*mrro*) were  
302 provided and analyzed. If daily outputs were not available, 3-hourly or 6-hourly outputs  
303 were averaged to daily and analyzed. Of the larger HighResMIP ensemble (19 models)  
304 only seven models (11 total simulations) provided, at least, Tier 1 simulations with daily  
305 SWE outputs. Of that subset of models, four models (seven total simulations) provided  
306 Tier 2 data with, at least, daily SWE. These model simulations were provided by the  
307 Centre National de Recherches Météorologiques, CNRM-CM6-1 (Voldoire et al., 2019;  
308 Voldoire, 2019a, 2019b)), ECMWF consortium member states, EC-Earth3P (R. Haarsma  
309 et al., 2020; Consortium, 2018, 2019)), and Meteorological Research Institute, MRI-AGCM3-  
310 2 (Mizuta et al., 2012, 2019a, 2019b). Notably, one of the Tier 2 simulations, NOAA-  
311 GFDL-CM4C192, only provided daily SWE between 2035-2050 and is left out of the anal-  
312 ysis. The nominal resolution and ensemble member for each of the simulations used in  
313 this analysis are provided in Table S1. The only model to satisfy Tier 1-3 (MRI-AGCM3-  
314 2) was used for a more extensive analysis of the date-of- and degrees-to-emergence of low-  
315 to-no snow and its post-emergence implications on the mountainous hydrologic cycle.  
316 MRI-AGCM3-2 also provided some of the highest-resolution simulations (60 km and 20 km)  
317 in the HighResMIP ensemble and has shown above-median skill (total score of 82; top  
318 score was 85) across several Earth system model skill indicators, spanning the energy bud-  
319 get, hydrologic cycle, large-scale dynamics, and seasonal metrics (Fasullo, 2020).

320 There is a growing literature that shows Earth system model simulations run at  
321 sufficiently high-resolution ( $\leq 0.5^\circ$  horizontal resolution), like those provided by High-  
322 ResMIP, show better convergence in the representation of the global hydrologic cycle,  
323 generally through better representation of topography, moisture transport, land-sea con-  
324 trasts and precipitation ratios, and less-reliance on subgrid-scale parameterizations to  
325 estimate precipitation (Demory et al., 2013). For example, enhanced topographic rep-  
326 resentation along the American Cordillera (namely in Central America) has also been  
327 shown to dampen long-standing global circulation biases, such as the double Intertrop-  
328 ical Convergence Zone (Baldwin et al., 2021), and has shown better representation in mountain-

329 range scale snowpack lifecycles when compared to low-resolution simulations (Rhoades  
330 et al., 2017, 2018; Kapnick et al., 2018). Although model convergence in the represen-  
331 tation of the seasonal cycle of mountain snowpack may require even higher-resolutions  
332 we also note that model fidelity does not always systematically increase with higher-resolutions  
333 alone (Rhoades et al., 2018).

334 With that said, the analysis was limited by the lack of Earth system models that  
335 simulated a future climate scenario to 2100 and output daily SWE to appropriately es-  
336 timate the peak amount and timing of water stored in mountain snowpacks. The weak  
337 signal-to-noise in changing snow conditions along the American Cordillera by 2050 and  
338 the stronger signal-to-noise post-2050 underscores the importance of producing contin-  
339 uous climate projections to, at least, 2100 in future HighResMIP ensembles. Therefore,  
340 a major limitation of this analysis is that we were constrained to using a single model  
341 to estimate the date-of- and degrees-to-emergence of low-to-no snow. The use of a sin-  
342 gle member, single model simulation does not allow for the assessment of uncertainty in  
343 future projections associated with intermodel structural and parameter uncertainty, such  
344 as climate sensitivity and/or internal variability, and how they might influence estimates  
345 of a low-to-no snow future (Hawkins & Sutton, 2009; Hawkins et al., 2016; Lehner et al.,  
346 2020). A prioritization of multiple ensemble members in future HighResMIP experiments  
347 would help to constrain uncertainties associated with internal variability and climate sen-  
348 sitivity. Uncertainty in our analysis also arises due to the use of a single-emissions sce-  
349 nario which does not account for rapid policy intervention that could limit greenhouse  
350 gas emissions (Williams et al., 2021). To sidestep emission scenario specific outcomes,  
351 we explicitly highlight both the global and local surface air temperatures at which low-  
352 to-no snow emergence might occur. With all of that said, we note that our analysis is  
353 a proof-of-concept of what future high-resolution multi-model ensembles could deliver.

### 354 **Mountain Definition**

355 The HighResMIP ensemble offers some of the most cutting-edge, high-resolution  
356 Earth system model simulations to date, particularly over centennial-scale time periods.  
357 The model horizontal resolutions across the three models used in our analysis spanned  
358  $\sim 250$  km to  $\sim 20$  km (Table S1). Yet, even at the horizontal resolutions offered in High-  
359 ResMIP, a central question to this analysis is how well the hypsometry of the American  
360 Cordillera is represented.

361 To evaluate the mountainous hydrologic cycle response to future asymmetric warm-  
 362 ing, we utilize a mountain mask that isolates the world’s mountains into 1,013 distinct  
 363 polygons comprising an area of 13.8 million km<sup>2</sup> (Körner et al., 2011, 2017). We sub-  
 364 set this larger mountain mask to only include the American Cordillera, which spans the  
 365 Pacific Coast Ranges of Alaska and British Columbia through the South American An-  
 366 des (Figure 5). The American Cordillera is ideal to assess hemispheric asymmetry to low-  
 367 to-no snow as it is contiguous across more latitude bands than any mountain range in  
 368 the world and is continuously abutted by the Pacific Ocean to its west ensuring that hy-  
 369 drologic cycle responses are not markedly influenced by upwind landmass interactions.

370 According to the Global Mountain Biodiversity Assessment (G MBA; [http://www](http://www.mountainbiodiversity.org/explore)  
 371 [.mountainbiodiversity.org/explore](http://www.mountainbiodiversity.org/explore)), orchestrated by Körner et al. (2017), a mean  
 372 latitude-band elevation between 83m to 3498m, a maximum latitude-band elevation of  
 373 6261m (based on the ~4 km resolution Shuttle Radar Topography Mission elevation dataset)  
 374 and a maximum ruggedness of 1154m (maximal elevational difference among 3 x 3 grid).  
 375 Comparatively, the highest-resolution model in the HighResMIP ensemble (MRI-AGCM3-  
 376 2-S) has a nearly exact representation of the mean latitude-band elevation (between 28m  
 377 and 3497m) as G MBA, yet there is a ~1000m low-bias in the maximum latitude-band  
 378 elevation of 5294m (Figure 5).

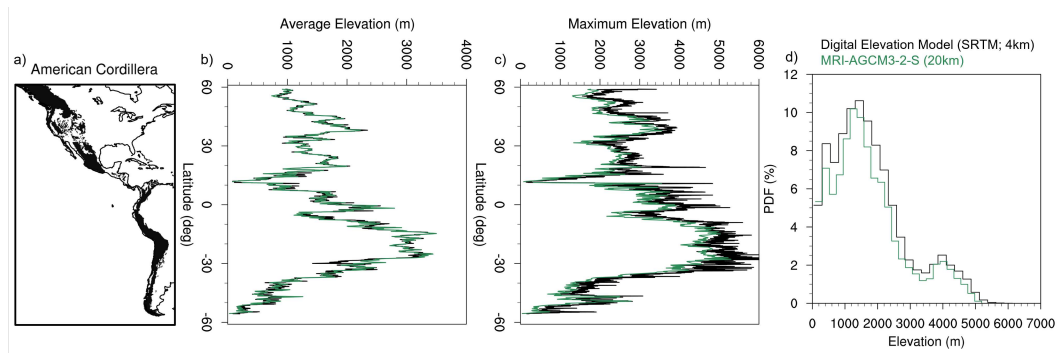


**Figure 5.** a) the American Cordillera mountain region (black shaded region on map). b) latitude-band mean and c) latitude-band maximum elevation along the American Cordillera. d) the distribution of elevations along the American Cordillera. Shuttle Radar Topography Mission (SRTM; <https://srtm.csi.cgiar.org/>) digital elevation model estimates (4 km; black) and MRI-AGCM3-2-S topography (20 km; dark green) are shown.

## 379 **Historical Validation of HighResMIP**

380 To evaluate historical skill across the six HighResMIP simulations used for this anal-  
381 ysis we provide a brief comparison with the fifth-generation of the European Centre for  
382 Medium-Range Weather Forecasts (ECMWF) atmospheric reanalysis (ERA5; Coper-  
383 nicus Climate Change Service Climate Data Store, 2017). The mean climatological (1979-  
384 2014) averages for the Intermountain West and Chilean Andes of the American Cordillera  
385 in ERA5 and CNRM (Figure S13 and S16), EC-Earth3P (Figure S14 and S17), and MRI  
386 (Figure S15 and S18) are provided in the Supplemental Material. The variables analyzed  
387 coincide with those presented in the analysis of future projections, namely annual mean  
388 surface air temperature, annual total precipitation, peak SWE, and annual total runoff.  
389 The variables are also masked with the American Cordillera mask at their native res-  
390 olutions. Summary statistics, namely annual median, spatial-mean median bias, mean,  
391 spatial-mean mean bias, and standard deviation, and the spatial-mean range of bias, are  
392 also provided (Table S2 and S3).

393 Relative to ERA5 all HighResMIP models have a cold-bias (mean bias between -  
394 0.4 to -1.4 °C relative to ERA5's 4.6 °C) in the Intermountain West that amplifies at  
395 higher-resolution (Table S2). Most models (4/6 simulations) also produce more precip-  
396 itation (mean bias between -108 mm to 215 mm relative to ERA5's 1120 mm), save for  
397 the EC-Earth3P simulations. The interactions between colder-than-expected surface air  
398 temperatures and higher-than-expected precipitation also result in larger-than-expected  
399 peak SWE for four of the six simulations (mean bias between -37 mm to 111 mm rel-  
400 ative to ERA5's 291 mm), save for the coarsest resolution simulations that have smaller  
401 snowfall fractions. All models produced larger amounts of runoff than ERA5 (mean bias  
402 of 92 mm to 450 mm relative to ERA5's 504 mm), particularly at higher-resolution and  
403 especially along the Pacific Coast Range of British Columbia.

404 In the Chilean Andes there is a comparable temperature-bias to the Intermoun-  
405 tain West (mean bias between -0.5 to 0.9 °C relative to ERA5's 5.7 °C) and for each low-  
406 and high-resolution model pair horizontal refinement leads to colder simulated temper-  
407 atures (Table S3). Akin to the Intermountain West, EC-Earth3P produces too little pre-  
408 cipitation and the rest of the simulations too much (mean bias between -407 mm to 276 mm  
409 relative to ERA5's 2460 mm). This is consistent with runoff (mean bias between -94 and  
410 1140 mm relative to ERA5's 1410 mm). Nearly all simulations have higher-than-expected

411 peak SWE (mean bias between -642 mm to 1810 mm relative to ERA5’s 701 mm). Sev-  
412 eral of the HighResMIP simulations, particularly in the Coast Range of British Columbia  
413 and the southern Chilean Andes, combine seasonal snowpack and perennial ice/glaciers  
414 into outputs of SWE (e.g., CNRM-CM6) that in turn influence historical comparisons  
415 of peak SWE and annual total runoff. Notably, across most hydroclimate variables and  
416 hemispheres MRI-AGCM3-2-S consistently had some of the smallest spatial-mean range  
417 of bias compared with ERA5, although with better skill in the Intermountain West than  
418 Chilean Andes.

### 419 **Calculation of the Date-of-Emergence of Low-to-No Snow**

420 To assess the hemispheric asymmetry and latitudinal responses of the American  
421 Cordillera to climate change we assess annual maximum snow water equivalent (SWE),  
422 or peak SWE. Peak SWE is calculated for the entirety of the HighResMIP model sim-  
423 ulation period (1950-2099) and averaged across each latitude band within the American  
424 Cordillera. To eliminate regions of ephemeral snow cover, a minimum amount of peak  
425 SWE depth was needed ( $>2.54$  mm; or the instrumental precision of in-situ SWE mea-  
426 surements, [https://www.nrcs.usda.gov/wps/portal/wcc/home/dataAccessHelp/faqs/  
427 snotelSensors/](https://www.nrcs.usda.gov/wps/portal/wcc/home/dataAccessHelp/faqs/snotelSensors/)). We then bin filtered peak SWE estimates into 10th percentile bins,  
428 using the first 50 years of the simulation as the historical reference period (1950-2000).  
429 Importantly, this historical reference period is characterized by a wide range of climate  
430 variability indicators (e.g., strong to weak phases of the El Niño Southern Oscillation;  
431 Patricola et al., 2019).

432 To quantitatively isolate the persistence of low-to-no snow years we develop sev-  
433 eral definitions and apply them to the HighResMIP simulation over the American Cordillera.  
434 Low-snow is defined as peak SWE  $\leq$ 30th percentile and (virtually) no-snow is peak SWE  
435  $\leq$ 10th percentile (Siirila-Woodburn et al., 2021). These percentiles are also analogous  
436 to “snow drought” thresholds utilized in recent literature (e.g., Marshall et al., 2019;  
437 Hatchett et al., 2021), yet we prefer the low-to-no snow label as drought implies a tem-  
438 porary deviation from normal which is unlikely to occur in a dramatically warmer world.  
439 The low-to-no snow percentile-based definition is chosen based partly on the success of  
440 the Western US Drought Monitor’s ability to highlight impactful water stress in the land-  
441 scape (Svoboda et al., 2002; Huning & AghaKouchak, 2020b) and, more specifically, based  
442 on recent research which shows that runoff is reduced and consistently more constrained

443 in portions of the western US when peak SWE approaches conditions of low-to-no snow  
 444 (Sexstone et al., 2020; Hatchett et al., 2021).

445 We define a back-to-back low-to-no snow year as “extreme”, five years in a row as  
 446 “episodic”, and 10 years in a row as “persistent”. These temporal definitions are cho-  
 447 sen based on their historical impact on water management; namely, the ability of tra-  
 448 ditional management mechanisms and infrastructure storage capacities to meet annual  
 449 water demand (Siirila-Woodburn et al., 2021). Back-to-back (extreme) years of low-to-  
 450 no snow have occurred in the historical record, for example in the 1970s and 2010s (Mote  
 451 et al., 2018; Huning & AghaKouchak, 2020a). Although impactful, historically these con-  
 452 ditions were intermittent and not spatially ubiquitous across the western US, rarely lead-  
 453 ing to catastrophic water supply outcomes. Episodic low-to-no snow (five-years in a row)  
 454 has also occurred in recent history (2012-2016) in the western US and led to dramatic  
 455 shifts in water and agricultural management practices, new water policy (e.g., Sustain-  
 456 able Groundwater Act), and mandatory reductions in water use (Mote et al., 2016). Last,  
 457 persistent low-to-no snow (10-years in a row) has yet to occur in the historical record.  
 458 This would likely be virtually impossible to meet historical water demand assuming no  
 459 changes to water management practices and infrastructure.

Using both the low-to-no snow definition and the temporal definitions, we then estimate, at each latitude band (mean conditions) along the American Cordillera when peak SWE percentiles met (1) or didn’t meet (0) the  $\leq 30$ th percentile.

$$Y_t = \begin{cases} 1 & \text{if the peak SWE in year } t \text{ is } \leq 30\text{th percentile SWE,} \\ 0 & \text{otherwise,} \end{cases} \quad t = 1950 - 2099,$$

$$Z_t^{\text{Extr}} = \begin{cases} 1 & \text{if } Y_t = 1, Y_{t-1} = 1, \\ 0 & \text{otherwise,} \end{cases} \quad t = 1951 - 2099,$$

$$Z_t^{\text{Epis}} = \begin{cases} 1 & \text{if } Y_t = 1, \dots, Y_{t-4} = 1, \\ 0 & \text{otherwise,} \end{cases} \quad t = 1955 - 2099,$$

$$Z_t^{\text{Pers}} = \begin{cases} 1 & \text{if } Y_t = 1, \dots, Y_{t-9} = 1, \\ 0 & \text{otherwise,} \end{cases} \quad t = 1959 - 2099.$$

A common statistical analysis when dealing with data such as  $Z_t^{\text{Extr}}$ ,  $Z_t^{\text{Epis}}$ , and  $Z_t^{\text{Pers}}$  is that of logistic regression, which seeks to quantify relationships between some

independent or explanatory variable of interest (e.g., surface air temperature [tas];  $X_t$ ):

$$X_t = \text{tas value (K) in year } t, \quad t = 1950 - 2099,$$

460 and a dependent or response variable (e.g., low-to-no snow;  $Y_t$ ) that is  $\{0, 1\}$ . For sim-  
 461 plicity of notation, we drop the superscript and simply outline an analysis for  $Z_t$ , which  
 462 generically refers to extreme, episodic, and persistent low-to-no snow. Eventually, we will  
 463 fit a separate logistic regression to each of  $Z_t^{\text{Extr}}$ ,  $Z_t^{\text{Epis}}$ , and  $Z_t^{\text{Pers}}$ .

Unlike ordinary least squares regression, which quantifies linear relationships be-  
 tween an explanatory variable and some continuous response variable, logistic regression  
 instead quantifies a relationship between an arbitrary explanatory variable and the prob-  
 ability of the response variable being 1, denoted  $p_t = \text{Prob}(Z_t = 1)$ . However, since  
 probabilities are bounded by 0 and 1, the regression is conducted on the so-called “log  
 odds” of  $Z_t = 1$ , often referred to as the logit function, which is defined as:

$$\text{logit}(p_t) \equiv \log\left(\frac{p}{1-p}\right).$$

Importantly, for  $p_t \in (0, 1)$ , the  $\text{logit}(p_t) \in (-\infty, \infty)$ , which ensures that the estimated  
 probabilities lie between zero and one. In this case, we set up the logit statistical model  
 using the tas time series  $\{X_t : t = 1950, \dots, 2099\}$  as an explanatory variable as fol-  
 lows:

$$Z_t = \begin{cases} 1 & \text{with probability } p_t, \\ 0 & \text{with probability } 1 - p_t, \end{cases}$$

where we model

$$\text{logit}(p_t) = \beta_0 + \beta_1 X_t,$$

where  $X_t$  = the tas value in year  $t$ . Numerical methods are used to estimate the sta-  
 tistical parameters  $\{\beta_0, \beta_1\}$ , call these  $\{\hat{\beta}_0, \hat{\beta}_1\}$ , which can then be used to derive esti-  
 mated probabilities  $\hat{p}_t$  in each year using the inverse logit function

$$\hat{p}_t = \text{logit}^{-1}(\hat{\beta}_0 + \hat{\beta}_1 X_t) = \frac{\exp\{\hat{\beta}_0 + \hat{\beta}_1 X_t\}}{1 + \exp\{\hat{\beta}_0 + \hat{\beta}_1 X_t\}}.$$

464 We can then use these fitted probabilities to identify a date-of-emergence for each low-  
 465 to-no snow category: select the first year for which  $\hat{p}_t > 0.5$ . The 0.5 threshold is cho-  
 466 sen because it represents, at least, a greater than random chance of occurrence of the  
 467 various consecutive low-to-no snow year conditions.

## 468 Calculation of Hemispheric Warming and Meridional Circulation Changes

469 We utilize the analysis framework presented in Friedman et al. (2013) to show hemi-  
470 spheric asymmetries in both surface warming (Figure S3a,b) and meridional circulation  
471 (Figure S3c,d). Hemispheric annual mean surface air temperature anomalies from the  
472 1950-2000 reference period were computed for MRI-AGCM3-2-S and is consistent across  
473 all six HighResMIP simulations (not shown). For the meridional circulation we compute  
474 stream functions at 6-hourly frequencies using surface pressure and meridional winds across  
475 the seven pressure levels available. Due to 6-hourly output limitations in CNRM-CM6-  
476 1 and EC-Earth3P (e.g., surface pressure) meridional circulations could only be computed  
477 for MRI-AGCM3-2-S, although results are consistent across all six HighResMIP simu-  
478 lations using monthly outputs (not shown). Pressure levels include (units of Pa): 92500,  
479 85000, 70000, 60000, 50000, 25000, 5000. We then take the 6-hourly stream functions  
480 and compute annual means and calculate a reference period climatology (1950-2000). The  
481 maximum streamfunction across all pressure levels is then identified and differenced for  
482 each year from the reference period. These values are then converted from kg/s to Sver-  
483 drups (Sv) by multiplying by  $1 \times 10^{-9}$ . We then compute latitudinal averages of the dSv  
484 values. Finally, we difference the Southern Hemisphere values from the Northern Hemi-  
485 sphere values to more clearly isolate the hemispheric asymmetry.

486 The findings of this study regarding an asymmetric response in hemispheric sur-  
487 face air temperature and meridional overturning circulation are corroborated by the pa-  
488 leoclimate record (Putnam & Broecker, 2017), the observational record (Xu & Ramanathan,  
489 2012), and other modeling experiments (Friedman et al., 2013). Since the 1980s, obser-  
490 vations show that the Northern Hemisphere has warmed faster than the Southern Hemi-  
491 sphere, largely as a result of differences in sea-to-land fraction and polar amplification  
492 (Xu & Ramanathan, 2012). This hemispheric asymmetry in warming has altered the gen-  
493 eral circulation of the atmosphere and the location, variability and persistence of the storm  
494 track (Held & Soden, 2006; Putnam & Broecker, 2017; Allan et al., 2020). Future warm-  
495 ing exacerbates this asymmetry, as shown by Friedman et al. (2013) using two genera-  
496 tions of a multi-model ensemble. These model projections show a significant weakening  
497 of the Hadley Circulation in the Northern Hemisphere and a slight strengthening in the  
498 Southern Hemisphere by 2100 associated with disproportionate warming over Northern  
499 Hemisphere landmasses and the Arctic. Differential alterations to the Hadley Circula-  
500 tion have implications for jet stream dynamics that act as first-order controls on regional

501 scale variability in cyclone and blocking events (Screen & Simmonds, 2014; Röthlisberger  
502 et al., 2016). This synoptic-scale variability directly connects to the frequency and in-  
503 tensity of landfalling storms that undergo orographic uplift and subsequently produce  
504 precipitation and build seasonal snowpacks. In the coastal midlatitudes, many such storm  
505 events presently occur at or near freezing temperatures (Bales et al., 2006), implying any  
506 warming may have an outsized influence on the amount of mountain water storage and  
507 the timing of runoff.

## 508 **Acknowledgments**

509 This study was funded by the Director, Office of Science, Office of Biological and En-  
510 vironmental Research of the U.S. Department of Energy Regional and Global Climate  
511 Modeling Program (RGCM) “the Calibrated and Systematic Characterization, Attri-  
512 bution and Detection of Extremes (CASCADE)” Science Focus Area (award no. DE-  
513 AC02-05CH11231) and the “An Integrated Evaluation of the Simulated Hydroclimate  
514 System of the Continental US” project (award no. DE-SC0016605). Analysis and model  
515 simulations were performed using the National Energy Research Scientific Computing  
516 Center (NERSC), specifically Cori-Haswell and Cori-KNL supercomputing facilities.

517 We acknowledge the World Climate Research Programme, which, through its Work-  
518 ing Group on Coupled Modelling, coordinated and promoted CMIP6. We thank the cli-  
519 mate modeling groups for producing and making available their model output, the Earth  
520 System Grid Federation (ESGF) for archiving the data and providing access, and the  
521 multiple funding agencies who support CMIP6 and ESGF. We also thank DOE’s RGMA  
522 program area, the Data Management program, and NERSC for making this coordinated  
523 CMIP6 analysis activity possible.

## 524 **Author Contributions:**

525 AMR conceived the study and led all analyses, figure generation, and writing. BJH,  
526 MDR, and ADJ supported the analyses and figure generation. WDC garnered and cu-  
527 rated the data. All authors contributed to the interpretation of study results and edit-  
528 ing of the study’s writing and figures.

## 529 **Corresponding Author:**

530 Correspondence to Alan M. Rhoades (arhoades@lbl.gov)

## 531 **Competing Interests:**

532 The authors declare no competing financial interests.

## 533 **References**

- 534 Allan, R. P., Barlow, M., Byrne, M. P., Cherchi, A., Douville, H., Fowler, H. J., ...  
535 Zolina, O. (2020). Advances in understanding large-scale responses of the  
536 water cycle to climate change. *Annals of the New York Academy of Sciences*,  
537 *1472*(1), 49-75. doi: <https://doi.org/10.1111/nyas.14337>
- 538 Amatulli, G., Domisch, S., Tuanmu, M.-N., Parmentier, B., Ranipeta, A., Malczyk,  
539 J., & Jetz, W. (2018). A suite of global, cross-scale topographic variables for  
540 environmental and biodiversity modeling. *Scientific data*, *5*(1), 1–15. doi:  
541 <https://doi.org/10.1038/sdata.2018.40>
- 542 Baldwin, J. W., Atwood, A. R., Vecchi, G. A., & Battisti, D. S. (2021). Outsize  
543 Influence of Central American Orography on Global Climate. *AGU Advances*,  
544 *2*(2), e2020AV000343. doi: <https://doi.org/10.1029/2020AV000343>
- 545 Bales, R. C., Molotch, N. P., Painter, T. H., Dettinger, M. D., Rice, R., & Dozier, J.  
546 (2006). Mountain hydrology of the western United States. *Water Resources*  
547 *Research*, *42*(8). doi: <https://doi.org/10.1029/2005WR004387>
- 548 Bambach, N. E., Rhoades, A. M., Hatchett, B. J., Jones, A. D., Ullrich, P. A., &  
549 Zarzycki, C. M. (2021). Projecting climate change in South America using  
550 variable-resolution Community Earth System Model: An application to Chile.  
551 *International Journal of Climatology*, 1-29. doi: [https://doi.org/10.1002/](https://doi.org/10.1002/joc.7379)  
552 [joc.7379](https://doi.org/10.1002/joc.7379)
- 553 Barry, R. G. (1992). Mountain weather and climate. *Cambridge University Press*.
- 554 Benjamini, Y., & Hochberg, Y. (1995). Controlling the False Discovery Rate:  
555 A Practical and Powerful Approach to Multiple Testing. *Journal of the*  
556 *Royal Statistical Society. Series B (Methodological)*, *57*(1), 289–300. doi:  
557 <http://www.jstor.org/stable/2346101>
- 558 Berghuijs, W., Woods, R., & Hrachowitz, M. (2014). A precipitation shift from snow  
559 towards rain leads to a decrease in streamflow. *Nature climate change*, *4*(7),  
560 583–586. doi: <https://doi.org/10.1038/nclimate2246>
- 561 Castilla-Rho, J., Rojas, R., Andersen, M., Holley, C., & Mariethoz, G. (2019).  
562 Sustainable groundwater management: How long and what will it take?  
563 *Global Environmental Change*, *58*, 101972. doi: <https://doi.org/10.1016/>

564 j.gloenvcha.2019.101972

565 Cody, M. L., & Mooney, H. A. (1978). Convergence Versus Nonconvergence in  
566 Mediterranean-Climate Ecosystems. *Annual Review of Ecology and Systemat-*  
567 *ics*, 9(1), 265-321. doi: 10.1146/annurev.es.09.110178.001405

568 Colombo, R., Garzonio, R., Di Mauro, B., Dumont, M., Tuzet, F., Cogliati, S., ...  
569 Cremonese, E. (2019). Introducing Thermal Inertia for Monitoring Snowmelt  
570 Processes With Remote Sensing. *Geophysical Research Letters*, 46(8), 4308-  
571 4319. doi: <https://doi.org/10.1029/2019GL082193>

572 Consortium, E.-E. (2018). *EC-Earth-Consortium EC-Earth3P-HR model output pre-*  
573 *pared for CMIP6 HighResMIP*. Earth System Grid Federation. doi: 10.22033/  
574 ESGF/CMIP6.2323

575 Consortium, E.-E. (2019). *EC-Earth-Consortium EC-Earth3P model output prepared*  
576 *for CMIP6 HighResMIP*. Earth System Grid Federation. doi: 10.22033/ESGF/  
577 CMIP6.2322

578 Copernicus Climate Change Service Climate Data Store. (2017). *Coperni-*  
579 *cus Climate Change Service (C3S): ERA5: Fifth generation of ECMWF*  
580 *atmospheric reanalyses of the global climate*. Retrieved 2021-08-16, from  
581 [https://cds.climate.copernicus.eu/cdsapp#!/dataset/reanalysis-era5-](https://cds.climate.copernicus.eu/cdsapp#!/dataset/reanalysis-era5-pressure-levels?tab=overview)  
582 [-pressure-levels?tab=overview](https://cds.climate.copernicus.eu/cdsapp#!/dataset/reanalysis-era5-pressure-levels?tab=overview)

583 Cosgrove, W. J., & Loucks, D. P. (2015). Water management: Current and fu-  
584 ture challenges and research directions. *Water Resources Research*, 51(6),  
585 4823-4839. doi: <https://doi.org/10.1002/2014WR016869>

586 Delaney, C. J., Hartman, R. K., Mendoza, J., Dettinger, M., Delle Monache, L.,  
587 Jasperse, J., ... Evett, S. (2020). Forecast Informed Reservoir Operations  
588 Using Ensemble Streamflow Predictions for a Multipurpose Reservoir in North-  
589 ern California. *Water Resources Research*, 56(9), e2019WR026604. doi:  
590 <https://doi.org/10.1029/2019WR026604>

591 Demory, M., Vidale, P., Roberts, M., Berrisford, P., Strachan, J., Schiemann, R.,  
592 & Mizielinski, M. (2013). The role of horizontal resolution in simulating  
593 drivers of the global hydrological cycle. *Climate Dynamics*, 42, 2201-2225. doi:  
594 <https://doi.org/10.1007/s00382-013-1924-4>

595 di Castri, F. (1973). Climatographical comparisons between chile and the west-  
596 ern coast of north america. In F. di Castri & H. A. Mooney (Eds.), *Mediterr-*

597 *ranean type ecosystems: Origin and structure* (pp. 21–36). Berlin, Heidelberg:  
598 Springer Berlin Heidelberg. doi: 10.1007/978-3-642-65520-3\_3

599 Dillon, P., Stuyfzand, P., Grischek, T., Lluria, M., Pyne, R., Jain, R., . . . others  
600 (2019). Sixty years of global progress in managed aquifer recharge. *Hydrogeol-*  
601 *ogy journal*, *27*(1), 1–30. doi: <https://doi.org/10.1007/s10040-018-1841-z>

602 Eidhammer, T., Grubišić, V., Rasmussen, R., & Ikdea, K. (2018). Winter Precipi-  
603 tation Efficiency of Mountain Ranges in the Colorado Rockies Under Climate  
604 Change. *Journal of Geophysical Research: Atmospheres*, *123*(5), 2573-2590.  
605 doi: <https://doi.org/10.1002/2017JD027995>

606 Fasullo, J. T. (2020). Evaluating simulated climate patterns from the CMIP archives  
607 using satellite and reanalysis datasets using the Climate Model Assessment  
608 Tool (CMATv1). *Geoscientific Model Development*, *13*(8), 3627–3642. doi:  
609 [10.5194/gmd-13-3627-2020](https://doi.org/10.5194/gmd-13-3627-2020)

610 Friedman, A. R., Hwang, Y.-T., Chiang, J. C., & Frierson, D. M. (2013). In-  
611 terhemispheric temperature asymmetry over the twentieth century and  
612 in future projections. *Journal of Climate*, *26*(15), 5419–5433. doi:  
613 <https://doi.org/10.1175/JCLI-D-12-00525.1>

614 Garreaud, R. D., Boisier, J. P., Rondanelli, R., Montecinos, A., Sepúlveda, H. H.,  
615 & Veloso-Aguila, D. (2020). The Central Chile Mega Drought (2010–2018):  
616 A climate dynamics perspective. *International Journal of Climatology*, *40*(1),  
617 421-439. doi: <https://doi.org/10.1002/joc.6219>

618 Haarsma, R., Acosta, M., Bakhshi, R., Bretonnière, P.-A., Caron, L.-P., Castrillo,  
619 M., . . . Wyser, K. (2020). HighResMIP versions of EC-Earth: EC-Earth3P  
620 and EC-Earth3P-HR – description, model computational performance and  
621 basic validation. *Geoscientific Model Development*, *13*(8), 3507–3527. doi:  
622 [10.5194/gmd-13-3507-2020](https://doi.org/10.5194/gmd-13-3507-2020)

623 Haarsma, R. J., Roberts, M. J., Vidale, P. L., Senior, C. A., Bellucci, A., Bao, Q.,  
624 . . . von Storch, J.-S. (2016). High Resolution Model Intercomparison Project  
625 (HighResMIP v1.0) for CMIP6. *Geoscientific Model Development*, *9*(11),  
626 4185–4208. doi: [10.5194/gmd-9-4185-2016](https://doi.org/10.5194/gmd-9-4185-2016)

627 Hatchett, B. J., Rhoades, A. M., & McEvoy, D. J. (2021). Monitoring the Daily  
628 Evolution and Extent of Snow Drought. *Natural Hazards and Earth System*  
629 *Sciences Discussions*, *2021*, 1–29. doi: [10.5194/nhess-2021-193](https://doi.org/10.5194/nhess-2021-193)

- 630 Hawkins, E., Smith, R. S., Gregory, J. M., & Stainforth, D. A. (2016). Irreducible  
631 uncertainty in near-term climate projections. *Climate Dynamics*, *46*(11),  
632 3807–3819. doi: <https://doi.org/10.1007/s00382-015-2806-8>
- 633 Hawkins, E., & Sutton, R. (2009). The potential to narrow uncertainty in regional  
634 climate predictions. *Bulletin of the American Meteorological Society*, *90*(8),  
635 1095–1108. doi: <https://doi.org/10.1175/2009BAMS2607.1>
- 636 Held, I. M., & Soden, B. J. (2006). Robust responses of the hydrological cy-  
637 cle to global warming. *Journal of Climate*, *19*(21), 5686 - 5699. doi:  
638 10.1175/JCLI3990.1
- 639 Hock, R., Rasul, G., Adler, C., Cáceres, B., Gruber, S., Hirabayashi, Y., ... others  
640 (2019). *High Mountain Areas. In: IPCC Special Report on the Ocean and*  
641 *Cryosphere in a Changing Climate.* doi: [https://www.ipcc.ch/srocc/chapter/](https://www.ipcc.ch/srocc/chapter/chapter-2/)  
642 [chapter-2/](https://www.ipcc.ch/srocc/chapter/chapter-2/)
- 643 Humboldt, A. v., & Bonpland, A. (1807). Ideen zu einer geographie der pflanzen  
644 nebst einem naturgemälde der tropenländer. *Cotta, Tübingen.*
- 645 Huning, L. S., & AghaKouchak, A. (2020a). Approaching 80 years of snow wa-  
646 ter equivalent information by merging different data streams. *Scientific Data*,  
647 *7*(1), 1–11. doi: <https://doi.org/10.1038/s41597-020-00649-1>
- 648 Huning, L. S., & AghaKouchak, A. (2020b). Global snow drought hot spots and  
649 characteristics. *Proceedings of the National Academy of Sciences*, *117*(33),  
650 19753–19759. doi: 10.1073/pnas.1915921117
- 651 Huss, M., Bookhagen, B., Huggel, C., Jacobsen, D., Bradley, R., Clague, J., ...  
652 Winder, M. (2017). Toward mountains without permanent snow and ice.  
653 *Earth's Future*, *5*(5), 418-435. doi: 10.1002/2016EF000514
- 654 Immerzeel, W. W., Lutz, A. F., Andrade, M., Bahl, A., Biemans, H., Bolch, T., ...  
655 Baillie, J. E. (2020, jan). Importance and vulnerability of the world's water  
656 towers. *Nature*, *577*(7790), 364–369. doi: 10.1038/s41586-019-1822-y
- 657 Jennings, K., Winchell, T. S., Livneh, B., & Molotch, N. P. (2018). Spatial variation  
658 of the rain–snow temperature threshold across the Northern Hemisphere. *Na-*  
659 *ture Communications*, *9*(1). doi: 10.1038/s41467-018-03629-7
- 660 Kapnick, S. B., Yang, X., Vecchi, G. A., Delworth, T. L., Gudgel, R., Malyshev, S.,  
661 ... Margulis, S. A. (2018). Potential for western US seasonal snowpack predic-  
662 tion. *Proceedings of the National Academy of Sciences*, *115*(6), 1180–1185. doi:

663 10.1073/pnas.1716760115

664 Körner, C., Jetz, W., Paulsen, J., Payne, D., Rudmann-Maurer, K., & Spehn, E. M.  
665 (2017). A global inventory of mountains for bio-geographical applications.  
666 *Alpine Botany*, 127(1), 1–15. doi: <https://doi.org/10.1007/s00035-016-0182-6>

667 Körner, C., Paulsen, J., & Spehn, E. M. (2011). A definition of mountains and their  
668 bioclimatic belts for global comparisons of biodiversity data. *Alpine Botany*,  
669 121(2), 73–78. doi: <https://doi.org/10.1007/s00035-011-0094-4>

670 Lehner, F., Deser, C., Maher, N., Marotzke, J., Fischer, E. M., Brunner, L., ...  
671 Hawkins, E. (2020). Partitioning climate projection uncertainty with multiple  
672 large ensembles and CMIP5/6. *Earth System Dynamics*, 11(2), 491–508. doi:  
673 10.5194/esd-11-491-2020

674 Lehner, F., Wahl, E. R., Wood, A. W., Blatchford, D. B., & Llewellyn, D. (2017).  
675 Assessing recent declines in Upper Rio Grande runoff efficiency from a pale-  
676 oclimate perspective. *Geophysical Research Letters*, 44(9), 4124–4133. doi:  
677 <https://doi.org/10.1002/2017GL073253>

678 Li, D., Wrzesien, M. L., Durand, M., Adam, J., & Lettenmaier, D. P. (2017). How  
679 much runoff originates as snow in the western United States, and how will that  
680 change in the future? *Geophysical Research Letters*, 44(12), 6163–6172. doi:  
681 <https://doi.org/10.1002/2017GL073551>

682 Livneh, B., & Badger, A. M. (2020). Drought less predictable under declining fu-  
683 ture snowpack. *Nature Climate Change*, 10(5), 452–458. doi: <https://doi.org/10.1038/s41558-020-0754-8>

684

685 Lynn, E., Cuthbertson, A., He, M., Vasquez, J. P., Anderson, M. L., Coombe, P.,  
686 ... Hatchett, B. J. (2020). Technical note: Precipitation-phase partitioning  
687 at landscape scales to regional scales. *Hydrology and Earth System Sciences*,  
688 24(11), 5317–5328. doi: 10.5194/hess-24-5317-2020

689 Marshall, A. M., Abatzoglou, J. T., Link, T. E., & Tennant, C. J. (2019). Projected  
690 Changes in Interannual Variability of Peak Snowpack Amount and Timing in  
691 the Western United States. *Geophysical Research Letters*, 46(15), 8882–8892.  
692 doi: <https://doi.org/10.1029/2019GL083770>

693 Milly, P. C. D., Betancourt, J., Falkenmark, M., Hirsch, R. M., Kundzewicz,  
694 Z. W., Lettenmaier, D. P., & Stouffer, R. J. (2008). Stationarity Is  
695 Dead: Whither Water Management? *Science*, 319(5863), 573–574. doi:

- 696 10.1126/science.1151915
- 697 Milly, P. C. D., & Dunne, K. A. (2020). Colorado River flow dwindles as warming-  
698 driven loss of reflective snow energizes evaporation. *Science*, *367*(6483), 1252-  
699 1255. doi: 10.1126/science.aay9187
- 700 Mizuta, R., Yoshimura, H., Murakami, H., Matsueda, M., Endo, H., Ose, T., ...  
701 others (2012). Climate simulations using MRI-AGCM3. 2 with 20-km grid.  
702 *Journal of the Meteorological Society of Japan. Ser. II*, *90*, 233–258. doi:  
703 10.2151/jmsj.2012-A12
- 704 Mizuta, R., Yoshimura, H., Ose, T., Hosaka, M., & Yukimoto, S. (2019a). *MRI*  
705 *MRI-AGCM3-2-H model output prepared for CMIP6 HighResMIP*. Earth Sys-  
706 tem Grid Federation. doi: 10.22033/ESGF/CMIP6.10972
- 707 Mizuta, R., Yoshimura, H., Ose, T., Hosaka, M., & Yukimoto, S. (2019b). *MRI*  
708 *MRI-AGCM3-2-S model output prepared for CMIP6 HighResMIP*. Earth Sys-  
709 tem Grid Federation. doi: 10.22033/ESGF/CMIP6.6942
- 710 Mooney, H., Dunn, E., Shropshire, F., & Song, L. (1970). Vegetation Comparisons  
711 between the Mediterranean Climatic Areas of California and Chile. *Flora*,  
712 *159*(5), 480-496. doi: [https://doi.org/10.1016/S0367-2530\(17\)31053-8](https://doi.org/10.1016/S0367-2530(17)31053-8)
- 713 Mote, P. W., Li, S., Lettenmaier, D. P., Xiao, M., & Engel, R. (2018). Dramatic de-  
714 clines in snowpack in the western US. *Npj Climate and Atmospheric Science*,  
715 *1*(1), 1–6. doi: <https://doi.org/10.1038/s41612-018-0012-1>
- 716 Mote, P. W., Rupp, D. E., Li, S., Sharp, D. J., Otto, F., Uhe, P. F., ... Allen,  
717 M. R. (2016). Perspectives on the causes of exceptionally low 2015 snowpack  
718 in the western United States. *Geophysical Research Letters*, *43*(20), 10,980-  
719 10,988. doi: <https://doi.org/10.1002/2016GL069965>
- 720 Muñoz, A. A., Klock-Barría, K., Alvarez-Garretón, C., Aguilera-Betti, I., Gonzalez-  
721 Reyes, A., Lastra, J. A., ... LeQuesne, C. (2020). Water Crisis in Petorca  
722 Basin, Chile: The Combined Effects of a Mega-Drought and Water Manage-  
723 ment. *Water*, *12*(3). doi: 10.3390/w12030648
- 724 Overpeck, J. T., & Udall, B. (2020). Climate change and the aridification of North  
725 America. *Proceedings of the National Academy of Sciences*, *117*(22), 11856–  
726 11858. doi: 10.1073/pnas.2006323117
- 727 Palazzi, E., Mortarini, L., Terzago, S., & Von Hardenberg, J. (2019). Elevation-  
728 dependent warming in global climate model simulations at high spatial reso-

- 729 lution. *Climate Dynamics*, 52(5), 2685–2702. doi: <https://doi.org/10.1007/s00382-018-4287-z>
- 730
- 731 Patricola, C. M., O’Brien, J. P., Risser, M. D., Rhoades, A. M., O’Brien, T. A.,  
732 Ullrich, P. A., . . . Collins, W. D. (2019). Maximizing enso as a source  
733 of western us hydroclimate predictability. *Climate Dynamics*, 1-22. doi:  
734 10.1007/s00382-019-05004-8
- 735 Paulsen, J., & Körner, C. (2014). A climate-based model to predict potential tree-  
736 line position around the globe. *Alpine Botany*, 124(1), 1–12. doi: <https://doi.org/10.1007/s00035-014-0124-0>
- 737
- 738 Payne, A. E., Demory, M.-E., Leung, L. R., Ramos, A. M., Shields, C. A., Rutz,  
739 J. J., . . . Ralph, F. M. (2020). Responses and impacts of atmospheric rivers  
740 to climate change. *Nature Reviews Earth & Environment*, 1, 143–157. doi:  
741 <https://doi.org/10.1038/s43017-020-0030-5>
- 742 Pepin, N., Bradley, R. S., Diaz, H., Baraër, M., Caceres, E., Forsythe, N., . . . others  
743 (2015). Elevation-dependent warming in mountain regions of the world. *Nature*  
744 *climate change*, 5(5), 424–430. doi: <https://doi.org/10.1038/nclimate2563>
- 745 Putnam, A. E., & Broecker, W. S. (2017). Human-induced changes in the distribu-  
746 tion of rainfall. *Science Advances*, 3(5). doi: 10.1126/sciadv.1600871
- 747 Rhoades, A. M., Ullrich, P. A., & Zarzycki, C. M. (2017). Projecting 21st cen-  
748 tury snowpack trends in western USA mountains using variable-resolution  
749 CESM. *Climate Dynamics*, 50, 261-288. doi: <https://doi.org/10.1007/s00382-017-3606-0>
- 750
- 751 Rhoades, A. M., Ullrich, P. A., Zarzycki, C. M., Johansen, H., Margulis, S. A., Mor-  
752 rison, H., . . . Collins, W. D. (2018). Sensitivity of Mountain Hydroclimate  
753 Simulations in Variable-Resolution CESM to Microphysics and Horizontal Res-  
754 olution. *Journal of Advances in Modeling Earth Systems*, 10(6), 1357-1380.  
755 doi: <https://doi.org/10.1029/2018MS001326>
- 756 Roberts, M. J., Baker, A., Blockley, E. W., Calvert, D., Coward, A., Hewitt, H. T.,  
757 . . . Vidale, P. L. (2019). Description of the resolution hierarchy of the  
758 global coupled HadGEM3-GC3.1 model as used in CMIP6 HighResMIP  
759 experiments. *Geoscientific Model Development*, 12(12), 4999–5028. doi:  
760 10.5194/gmd-12-4999-2019
- 761 Roberts, M. J., Camp, J., Seddon, J., Vidale, P. L., Hodges, K., Vanniere, B., . . .

- 762 Ullrich, P. (2020). Impact of Model Resolution on Tropical Cyclone Simula-  
763 tion Using the HighResMIP–PRIMAVERA Multimodel Ensemble. *Journal of*  
764 *Climate*, 33(7), 2557-2583. doi: 10.1175/JCLI-D-19-0639.1
- 765 Röthlisberger, M., Pfahl, S., & Martius, O. (2016). Regional-scale jet waviness mod-  
766 ulates the occurrence of midlatitude weather extremes. *Geophysical Research*  
767 *Letters*, 43(20), 10,989-10,997. doi: <https://doi.org/10.1002/2016GL070944>
- 768 Scanlon, B. R., Reedy, R. C., Faunt, C. C., Pool, D., & Uhlman, K. (2016). Enhanc-  
769 ing drought resilience with conjunctive use and managed aquifer recharge in  
770 California and Arizona. *Environmental Research Letters*, 11(3), 035013. doi:  
771 10.1088/1748-9326/11/3/035013
- 772 Screen, J. A., & Simmonds, I. (2014). Amplified mid-latitude planetary waves favour  
773 particular regional weather extremes. *Nature Climate Change*, 4(8), 704–709.  
774 doi: <https://doi.org/10.1038/nclimate2271>
- 775 Serrano-Notivoli, R., Tejedor, E., Sarricolea, P., Meseguer-Ruiz, O., Vuille, M.,  
776 Fuentealba, M., & de Luis, M. (2021). Hydroclimatic variability in Santiago  
777 (Chile) since the 16th century. *International Journal of Climatology*, 41(S1),  
778 E2015-E2030. doi: <https://doi.org/10.1002/joc.6828>
- 779 Sexstone, G. A., Driscoll, J. M., Hay, L. E., Hammond, J. C., & Barnhart, T. B.  
780 (2020). Runoff sensitivity to snow depletion curve representation within a  
781 continental scale hydrologic model. *Hydrological Processes*, 34(11), 2365-2380.  
782 doi: <https://doi.org/10.1002/hyp.13735>
- 783 Shea, J. M., Whitfield, P. H., Fang, X., & Pomeroy, J. W. (2021). The Role of Basin  
784 Geometry in Mountain Snowpack Responses to Climate Change. *Frontiers in*  
785 *Water*, 3, 4. doi: 10.3389/frwa.2021.604275
- 786 Siirila-Woodburn, E., Rhoades, A. M., Hatchett, B. J., Huning, L., Szinai, J., Tague,  
787 C., ... Kaatz, L. (2021). Evidence of a low-to-no snow future and its impacts  
788 on water resources in the western United States. *Nature Reviews Earth and*  
789 *Environment*, *Accepted*. doi: 10.1038/s43017-021-00219-y
- 790 Smith, R. B. (2019). 100 Years of Progress on Mountain Meteorology Research. *Me-*  
791 *teorological Monographs*, 59, 20.1-20.73. doi: 10.1175/AMSMONOGRAPHS-D  
792 -18-0022.1
- 793 Sterle, K., Hatchett, B. J., Singletary, L., & Pohl, G. (2019, 06). Hydroclimate  
794 Variability in Snow-Fed River Systems: Local Water Managers' Perspectives

795 on Adapting to the New Normal. *Bulletin of the American Meteorological*  
796 *Society*, 100(6), 1031-1048. Retrieved from [https://doi.org/10.1175/](https://doi.org/10.1175/BAMS-D-18-0031.1)  
797 [BAMS-D-18-0031.1](https://doi.org/10.1175/BAMS-D-18-0031.1) doi: 10.1175/BAMS-D-18-0031.1

798 Sturm, M., Goldstein, M. A., & Parr, C. (2017). Water and life from snow: A tril-  
799 lion dollar science question. *Water Resources Research*, 53(5), 3534-3544. doi:  
800 10.1002/2017WR020840

801 Svoboda, M., LeComte, D., Hayes, M., Heim, R., Gleason, K., Angel, J., ...  
802 Stephens, S. (2002). The Drought Monitor. *Bulletin of the American Me-*  
803 *teorological Society*, 83(8), 1181–1190. doi: 10.1175/1520-0477-83.8.1181

804 Szinai, J. K., Deshmukh, R., Kammen, D. M., & Jones, A. D. (2020). Evaluating  
805 cross-sectoral impacts of climate change and adaptations on the energy-water  
806 nexus: a framework and California case study. *Environmental Research Let-*  
807 *ters*, 15(12), 124065. doi: 10.1088/1748-9326/abc378

808 Vicuña, S., Vargas, X., Boisier, J. P., Mendoza, P. A., Gómez, T., Vásquez, N., &  
809 Cepeda, J. (2021). Impacts of climate change on water resources in Chile.  
810 In B. Fernández & J. Gironás (Eds.), *Water resources of Chile* (pp. 347–363).  
811 Cham: Springer International Publishing. doi: 10.1007/978-3-030-56901-3\_19

812 Viviroli, D., Kummu, M., Meybeck, M., Kallio, M., & Wada, Y. (2020). Increasing  
813 dependence of lowland populations on mountain water resources. *Nature Sus-*  
814 *tainability*, 1–12. doi: <https://doi.org/10.1038/s41893-020-0559-9>

815 Voldoire, A. (2019a). *CNRM-CERFACS CNRM-CM6-1-HR model output prepared*  
816 *for CMIP6 HighResMIP*. Earth System Grid Federation. doi: 10.22033/ESGF/  
817 CMIP6.1387

818 Voldoire, A. (2019b). *CNRM-CERFACS CNRM-CM6-1 model output prepared for*  
819 *CMIP6 HighResMIP*. Earth System Grid Federation. doi: 10.22033/ESGF/  
820 CMIP6.1925

821 Voldoire, A., Saint-Martin, D., Sénési, S., Decharme, B., Alias, A., Chevallier, M.,  
822 ... Waldman, R. (2019). Evaluation of CMIP6 DECK Experiments With  
823 CNRM-CM6-1. *Journal of Advances in Modeling Earth Systems*, 11(7), 2177-  
824 2213. doi: <https://doi.org/10.1029/2019MS001683>

825 Wilks, D. S. (2016). “The Stippling Shows Statistically Significant Grid Points”:  
826 How Research Results are Routinely Overstated and Overinterpreted, and  
827 What to Do about It. *Bulletin of the American Meteorological Society*, 97(12),

828 2263–2273. doi: 10.1175/BAMS-D-15-00267.1  
829 Williams, J. H., Jones, R. A., Haley, B., Kwok, G., Hargreaves, J., Farbes, J., &  
830 Torn, M. S. (2021). Carbon-Neutral Pathways for the United States. *AGU*  
831 *Advances*, 2(1), e2020AV000284. doi: <https://doi.org/10.1029/2020AV000284>  
832 Woodhouse, C. A., & Pederson, G. T. (2018). Investigating Runoff Efficiency in  
833 Upper Colorado River Streamflow Over Past Centuries. *Water Resources Re-*  
834 *search*, 54(1), 286-300. doi: <https://doi.org/10.1002/2017WR021663>  
835 Xu, Y., & Ramanathan, V. (2012). Latitudinally asymmetric response of global  
836 surface temperature: Implications for regional climate change. *Geophysical Re-*  
837 *search Letters*, 39(13). doi: <https://doi.org/10.1029/2012GL052116>

## Supplemental Material

**Table S1.** The ECMWF Reanalysis version 5 (ERA5) and High-Resolution Model Intercomparison Project (HighResMIP) models used for this analysis. Output variables are presented according to Climate Model Output Rewriter (CMOR) protocols including: mrro (surface runoff), orog (topography), pr (precipitation), prsn (snowfall), snw (snow water equivalent), and tas (surface air temperature).

<i>Model Name</i>	<i>Nominal Resolution</i>	<i>Latitude x Longitude</i>	<i>Ensemble Member</i>	<i>Time Period</i>	<i>Output Variable</i>
<b>GMBA</b>	4km	4320 x 8640			<i>orog</i>
<b>ERA5</b>	25km	720 x 1440		1979-2014	<i>snw tas pr mrro</i>
<b>CNRM-CM6-1</b>	250km	128 x 256	r1i1p1f2	1950-2050	<i>orog snw tas pr prsn mrro</i>
<b>CNRM-CM6-1-HR</b>	50km	360 x 720	r1i1p1f2	1950-2050	<i>orog snw tas pr prsn mrro</i>
<b>EC-Earth3P</b>	100km	256 x 512	r2i1p1f1	1950-2050	<i>orog snw tas pr prsn mrro</i>
<b>EC-Earth3P-HR</b>	50km	512 x 1024	r2i1p1f1	1950-2050	<i>orog snw tas pr prsn mrro</i>
<b>MRI-AGCM3-2-H</b>	60km	320 x 640	r1i1p1f1	1950-2100	<i>orog snw tas pr prsn mrro</i>
<b>MRI-AGCM3-2-S</b>	20km	960 x 1920	r1i1p1f1	1950-2100	<i>orog snw tas pr prsn mrro</i>

**Table S2.** The ECMWF Reanalysis version 5 (ERA5) and High-Resolution Model Intercomparison Project (HighResMIP) model summary statistics for the 1979-2014 annual mean surface air temperature (tas; °C), total precipitation (pr; mm), peak snow water equivalent (snw; mm), and total runoff (mrro; mm) within the Intermountain West (32° N to 59° N) of the American Cordillera. Annual spatial mean bias (model - ERA5) is given in parentheses for the 36-year period of 1979-2014. The range of bias is given in parentheses next to the annual mean standard deviations. Note that HighResMIP models vary in the inclusion of glacier/land ice in snw which can skew the summary statistics.

<i>Model Name</i>	<i>Median</i>	<i>Mean</i>	<i>Standard Deviation</i>
<b>tas</b>			
<b>ERA5</b>	3.9	4.6	5.2
<b>CNRM-CM6-1</b>	3.2 (-0.2)	4.2 (-0.4)	5.0 (2.2)
<b>CNRM-CM6-1-HR</b>	2.7 (-1.4)	3.2 (-1.4)	4.9 (2.5)
<b>EC-Earth3P</b>	3.1 (-0.7)	3.9 (-0.7)	5.3 (2.8)
<b>EC-Earth3P-HR</b>	2.9 (-0.9)	3.7 (-0.9)	5.1 (2.0)
<b>MRI-AGCM3-2-H</b>	2.7 (-1.0)	3.5 (-1.1)	4.9 (2.3)
<b>MRI-AGCM3-2-S</b>	2.5 (-1.4)	3.3 (-1.3)	5.1 (2.1)
<b>pr</b>			
<b>ERA5</b>	828	1120	836
<b>CNRM-CM6-1</b>	1000 (39)	1180 (57)	709 (444)
<b>CNRM-CM6-1-HR</b>	1080 (215)	1350 (234)	900 (371)
<b>EC-Earth3P</b>	791 (-108)	1010 (-108)	674 (299)
<b>EC-Earth3P-HR</b>	755 (-135)	1000 (-114)	730 (338)
<b>MRI-AGCM3-2-H</b>	928 (63)	1190 (69)	850 (356)
<b>MRI-AGCM3-2-S</b>	908 (109)	1240 (119)	1010 (313)
<b>snw</b>			
<b>ERA5</b>	180	291	806
<b>CNRM-CM6-1</b>	166 (-31)	253 (-37)	272 (242)
<b>CNRM-CM6-1-HR</b>	249 (106)	400 (109)	733 (60)
<b>EC-Earth3P</b>	247 (60)	352 (61)	349 (212)
<b>EC-Earth3P-HR</b>	249 (109)	401 (111)	675 (229)
<b>MRI-AGCM3-2-H</b>	184 (-30)	262 (-29)	287 (184)
<b>MRI-AGCM3-2-S</b>	183 (110)	391 (100)	980 (171)
<b>mrro</b>			
<b>ERA5</b>	345	504	561
<b>CNRM-CM6-1</b>	590 (282)	780 (276)	685 (426)
<b>CNRM-CM6-1-HR</b>	671 (444)	953 (450)	883 (355)
<b>EC-Earth3P</b>	397 (102)	595 (92)	619 (373)
<b>EC-Earth3P-HR</b>	365 (102)	606 (103)	699 (379)
<b>MRI-AGCM3-2-H</b>	330 (112)	624 (120)	792 (303)
<b>MRI-AGCM3-2-S</b>	319 (176)	688 (185)	936 (284)

**Table S3.** The ECMWF Reanalysis version 5 (ERA5) and High-Resolution Model Inter-comparison Project (HighResMIP) model summary statistics for the 1979-2014 annual mean surface air temperature (tas; °C), total precipitation (pr; mm), peak snow water equivalent (snw; mm), and total runoff (mrro; mm) within the Chilean Andes (32° S to 59° S) of the American Cordillera. Annual spatial mean bias (model - ERA5) is given in parentheses for the 36-year period of 1979-2014. The range of bias is given in parentheses next to the annual mean standard deviations. Note that HighResMIP models vary in the inclusion of glacier/land ice in snw and can skew the summary statistics.

<i>Model Name</i>	<i>Median</i>	<i>Mean</i>	<i>Standard Deviation</i>
<b>tas</b>			
<b>ERA5</b>	5.5	5.7	3.7
<b>CNRM-CM6-1</b>	5.9 (0.9)	6.7 (1.0)	3.2 (1.5)
<b>CNRM-CM6-1-HR</b>	4.8 (-0.5)	5.1 (-0.6)	4.3 (1.5)
<b>EC-Earth3P</b>	5.1 (-0.1)	5.6 (-0.1)	3.6 (2.1)
<b>EC-Earth3P-HR</b>	4.7 (-0.5)	5.1 (-0.6)	4.1 (1.6)
<b>MRI-AGCM3-2-H</b>	5.0 (0.1)	5.7 (0.1)	3.9 (1.3)
<b>MRI-AGCM3-2-S</b>	4.9 (-0.5)	5.2 (-0.4)	4.2 (1.6)
<b>pr</b>			
<b>ERA5</b>	2150	2460	1560
<b>CNRM-CM6-1</b>	2300 (80)	2560 (97)	1150 (920)
<b>CNRM-CM6-1-HR</b>	2850 (596)	3070 (615)	1570 (1100)
<b>EC-Earth3P</b>	1810 (-381)	2050 (-407)	1230 (874)
<b>EC-Earth3P-HR</b>	2030 (-167)	2300 (-157)	1420 (667)
<b>MRI-AGCM3-2-H</b>	2440 (236)	2690 (234)	1700 (948)
<b>MRI-AGCM3-2-S</b>	2160 (268)	2730 (276)	2270 (1010)
<b>snw</b>			
<b>ERA5</b>	185	701	1810
<b>CNRM-CM6-1</b>	10 (-627)	60 (-642)	113 (220)
<b>CNRM-CM6-1-HR</b>	92 (1860)	2510 (1810)	14500 (1750)
<b>EC-Earth3P</b>	139 (-440)	263 (-439)	320 (397)
<b>EC-Earth3P-HR</b>	227 (315)	1010 (310)	2300 (247)
<b>MRI-AGCM3-2-H</b>	37 (-474)	222 (-479)	835 (298)
<b>MRI-AGCM3-2-S</b>	34 (-25)	662 (-40)	2220 (235)
<b>mrro</b>			
<b>ERA5</b>	1010	1410	1300
<b>CNRM-CM6-1</b>	1680 (637)	2040 (624)	1180 (954)
<b>CNRM-CM6-1-HR</b>	2300 (1140)	2560 (1140)	1550 (1090)
<b>EC-Earth3P</b>	1120 (-100)	1320 (-94)	1080 (685)
<b>EC-Earth3P-HR</b>	1140 (94)	1540 (120)	1270 (571)
<b>MRI-AGCM3-2-H</b>	1440 (505)	1890 (476)	1640 (879)
<b>MRI-AGCM3-2-S</b>	1140 (540)	1940 (526)	2110 (906)

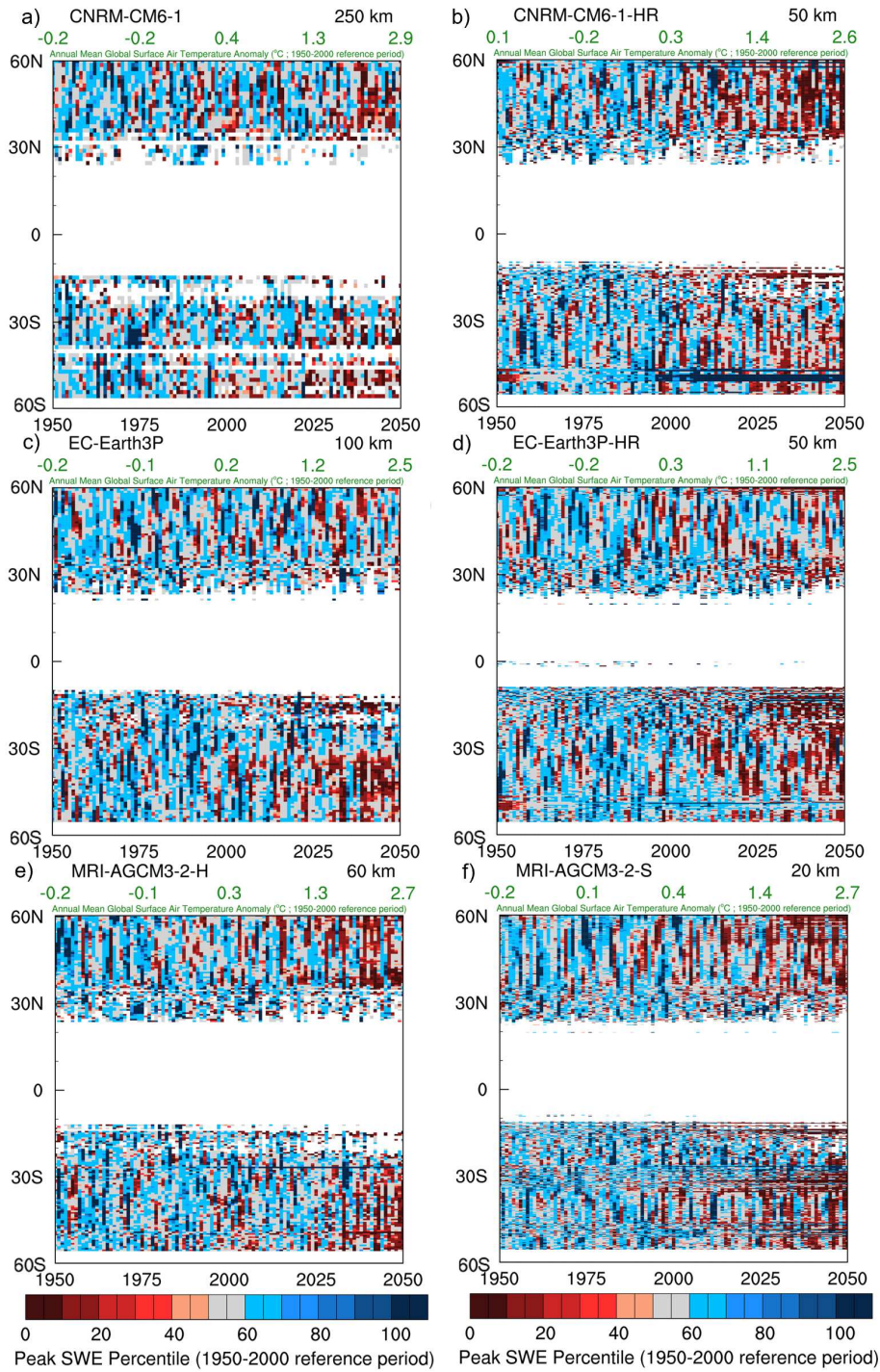


**Figure S1.** Annual peak snow water equivalent (SWE) percentiles within the American Cordillera ( $60^{\circ}$  N to  $60^{\circ}$  S) across six HighResMIP simulations over 1950-2050 under the high-emissions shared socioeconomic pathway (SSP585). The top x-axis shows the annual mean global surface air temperature anomalies and the bottom x-axis indicates the dates between 1950-2050. 1950-2000 is used as the historical reference period to compute percentile bins and annual mean surface air temperature anomalies. Low-to-no snow conditions are defined as annual peak SWE  $\leq 30$ th percentile.

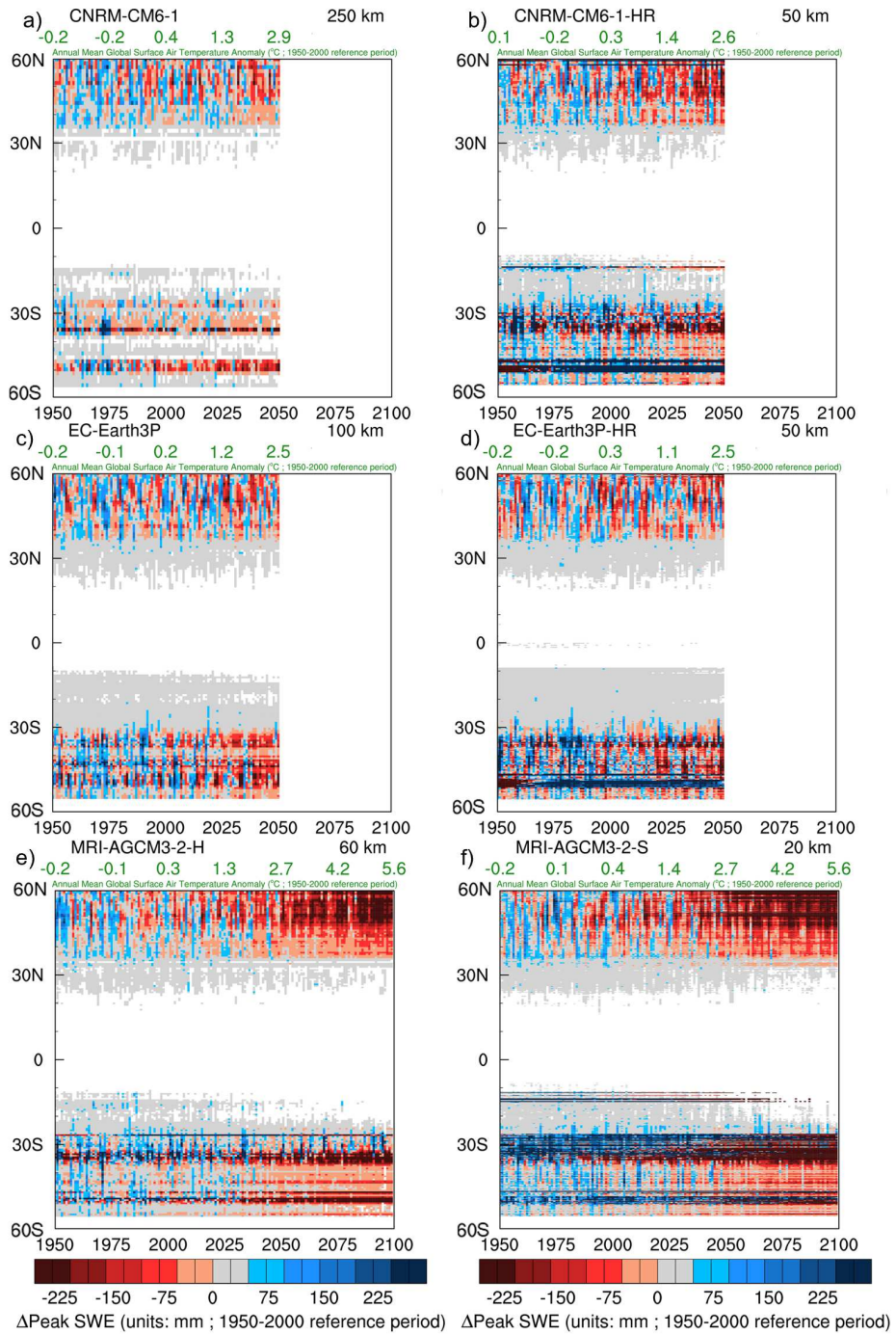


**Figure S2.** Same as in Figure S1, however the magnitude of peak SWE change (in mm) is shown relative to the historical reference period (1950-2000).

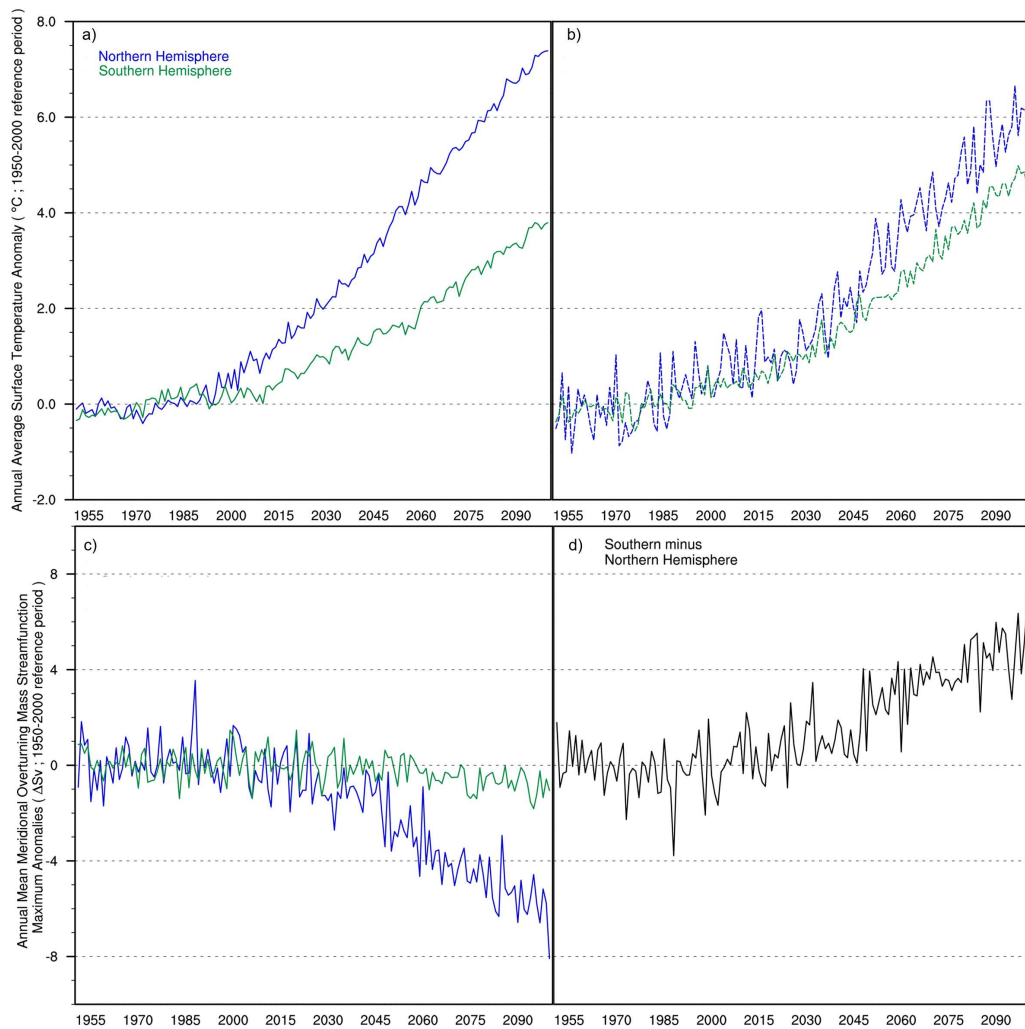


**Figure S3.** a) Northern (blue) and Southern (green) Hemisphere annual mean surface air temperature anomalies simulated by MRI-AGCM3-2-S. 1950-2000 is used as the historical reference period. b) shows only American Cordillera changes. c) shows the difference in annual mean maximum meridional overturning mass streamfunction from the historical reference period, analogous to Friedman et al. (2013). d) shows the circulation differences (Southern - Northern Hemisphere) between hemispheres in c).

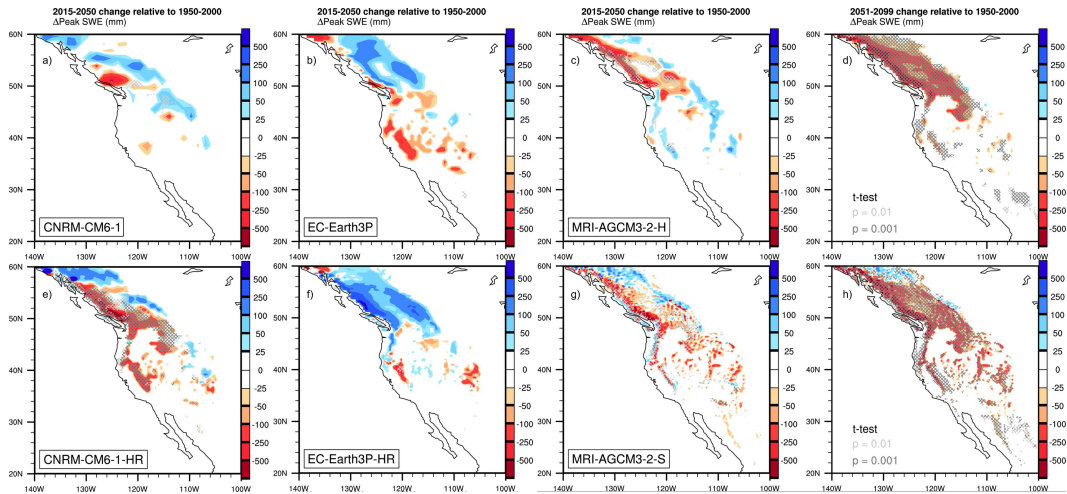


**Figure S4.** Mean peak SWE changes across the six HighResMIP simulations for 2015-2050 relative to 1950-2000 across the Intermountain West portion of the American Cordillera. The far right column of panel plots are mean peak SWE changes for the two simulations (MRI-AGCM3-2) that provided projections of 2051-2099, also relative to 1950-2000. Stippling indicates statistical significance using a two-tailed Student's t-test adjusted for Type-1 errors (False Discovery Rate; Benjamini & Hochberg, 1995; Wilks, 2016) at either  $p=0.01$  (light gray) or  $p=0.001$  (dark gray).

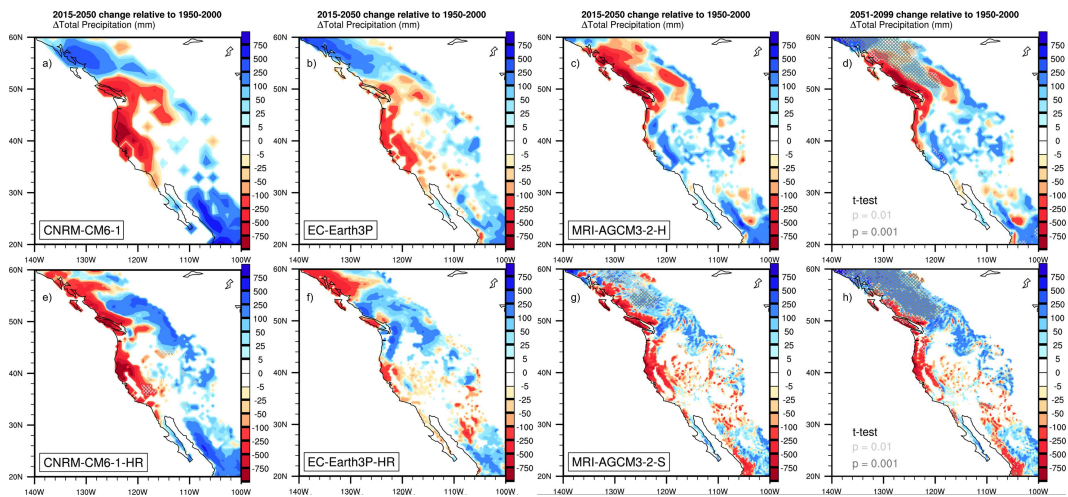


**Figure S5.** Annual mean total precipitation changes across the six HighResMIP simulations for 2015-2050 relative to 1950-2000 across the Intermountain West portion of the American Cordillera. The far right column of panel plots are annual mean total precipitation changes for the two simulations (MRI-AGCM3-2) that provided projections of 2051-2099, also relative to 1950-2000. Stippling indicates statistical significance using a two-tailed Student's t-test adjusted for Type-1 errors (False Discovery Rate; Benjamini & Hochberg, 1995; Wilks, 2016) at either  $p=0.01$  (light gray) or  $p=0.001$  (dark gray).

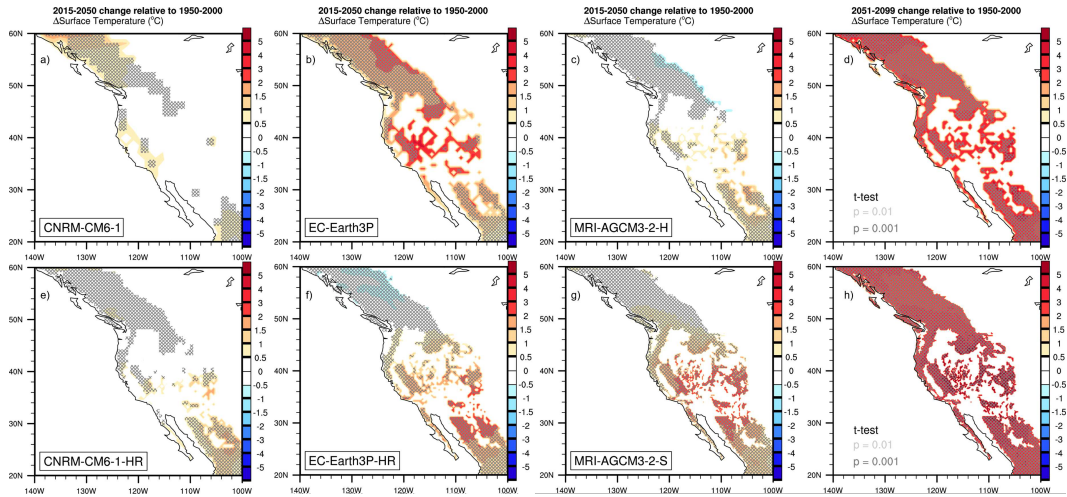


**Figure S6.** Annual mean surface air temperature changes across the six HighResMIP simulations for 2015-2050 relative to 1950-2000 across the Intermountain West portion of the American Cordillera. The far right column of panel plots are annual mean surface air temperature changes for the two simulations (MRI-AGCM3-2) that provided projections of 2051-2099, also relative to 1950-2000. Stippling indicates statistical significance using a two-tailed Student’s t-test adjusted for Type-1 errors (False Discovery Rate; Benjamini & Hochberg, 1995; Wilks, 2016) at either  $p=0.01$  (light gray) or  $p=0.001$  (dark gray).

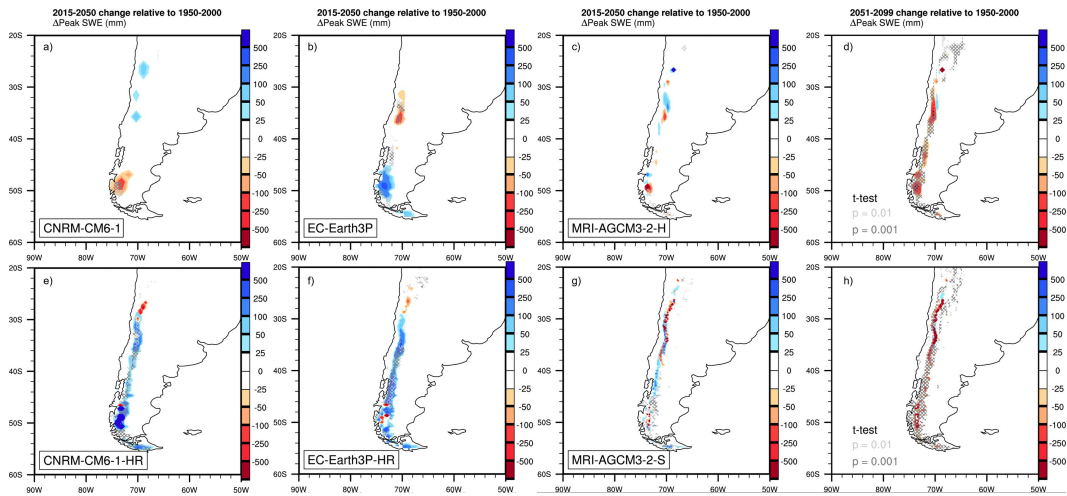


**Figure S7.** Mean peak SWE changes across the six HighResMIP simulations for 2015-2050 relative to 1950-2000 across the Chilean Andes portion of the American Cordillera. The far right column of panel plots are mean peak SWE changes for the two simulations (MRI-AGCM3-2) that provided projections of 2051-2099, also relative to 1950-2000. Stippling indicates statistical significance using a two-tailed Student’s t-test adjusted for Type-1 errors (False Discovery Rate; Benjamini & Hochberg, 1995; Wilks, 2016) at either  $p=0.01$  (light gray) or  $p=0.001$  (dark gray).

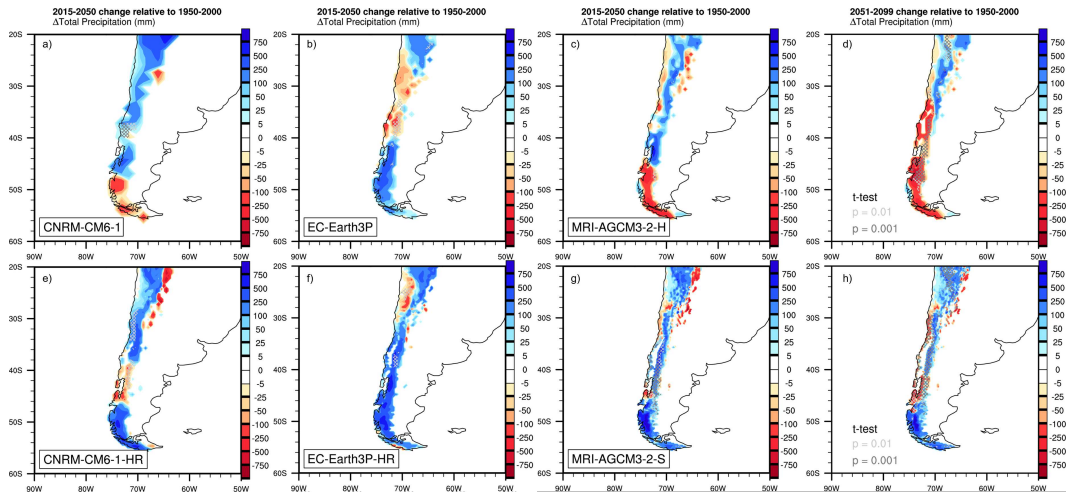


**Figure S8.** Annual mean total precipitation changes across the six HighResMIP simulations for 2015-2050 relative to 1950-2000 across the Chilean Andes portion of the American Cordillera. The far right column of panel plots are annual mean total precipitation changes for the two simulations (MRI-AGCM3-2) that provided projections of 2051-2099, also relative to 1950-2000. Stippling indicates statistical significance using a two-tailed Student's t-test adjusted for Type-1 errors (False Discovery Rate; Benjamini & Hochberg, 1995; Wilks, 2016) at either  $p=0.01$  (light gray) or  $p=0.001$  (dark gray).

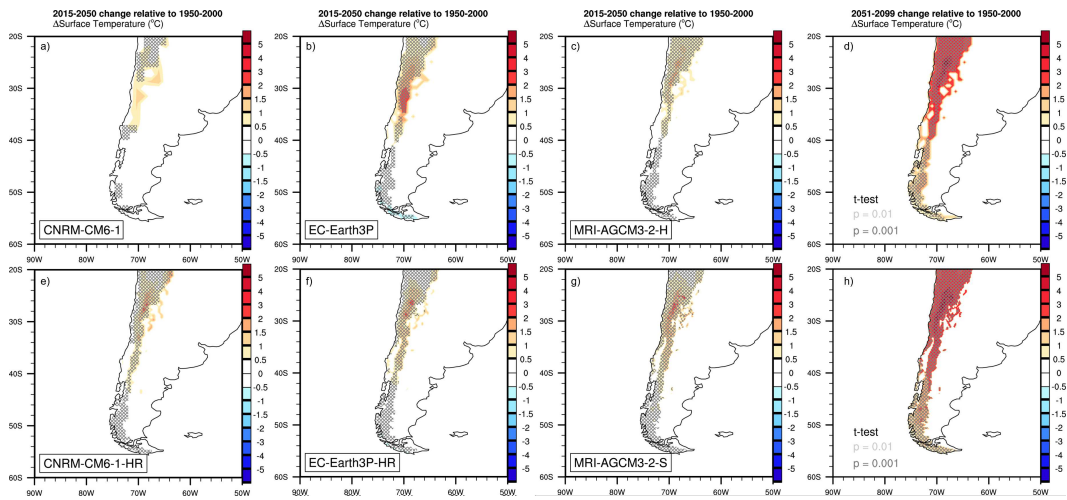


**Figure S9.** Annual mean surface air temperature changes across the six HighResMIP simulations for 2015-2050 relative to 1950-2000 across the Chilean Andes portion of the American Cordillera. The far right column of panel plots are annual mean surface air temperature changes for the two simulations (MRI-AGCM3-2) that provided projections of 2051-2099, also relative to 1950-2000. Stippling indicates statistical significance using a two-tailed Student’s t-test adjusted for Type-1 errors (False Discovery Rate; Benjamini & Hochberg, 1995; Wilks, 2016) at either  $p=0.01$  (light gray) or  $p=0.001$  (dark gray).

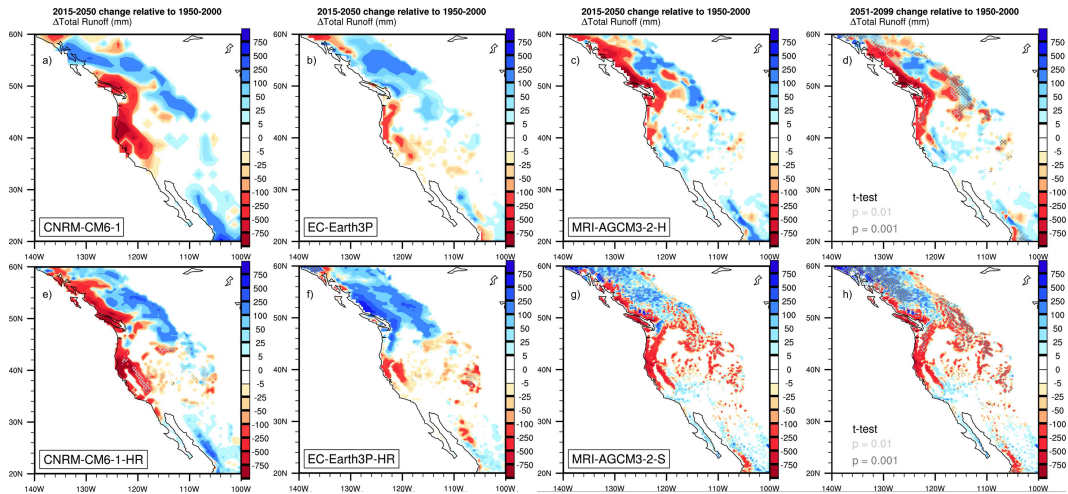


**Figure S10.** Annual mean total runoff changes across the six HighResMIP simulations for 2015-2050 relative to 1950-2000 across the Intermountain West portion of the American Cordillera. The far right column of panel plots are annual mean total runoff changes for the two simulations (MRI-AGCM3-2) that provided projections of 2051-2099, also relative to 1950-2000. Stippling indicates statistical significance using a two-tailed Student's t-test adjusted for Type-1 errors (False Discovery Rate; Benjamini & Hochberg, 1995; Wilks, 2016) at either  $p=0.01$  (light gray) or  $p=0.001$  (dark gray).

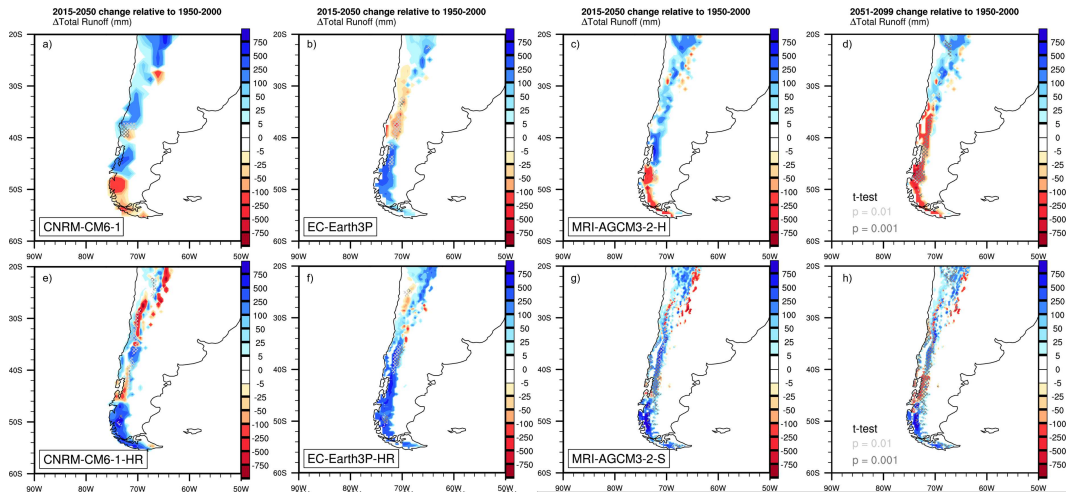


**Figure S11.** Annual mean total runoff changes across the six HighResMIP simulations for 2015-2050 relative to 1950-2000 across the Chilean Andes portion of the American Cordillera. The far right column of panel plots are annual mean total runoff changes for the two simulations (MRI-AGCM3-2) that provided projections of 2051-2099, also relative to 1950-2000. Stippling indicates statistical significance using a two-tailed Student's t-test adjusted for Type-1 errors (False Discovery Rate; Benjamini & Hochberg, 1995; Wilks, 2016) at either  $p=0.01$  (light gray) or  $p=0.001$  (dark gray).

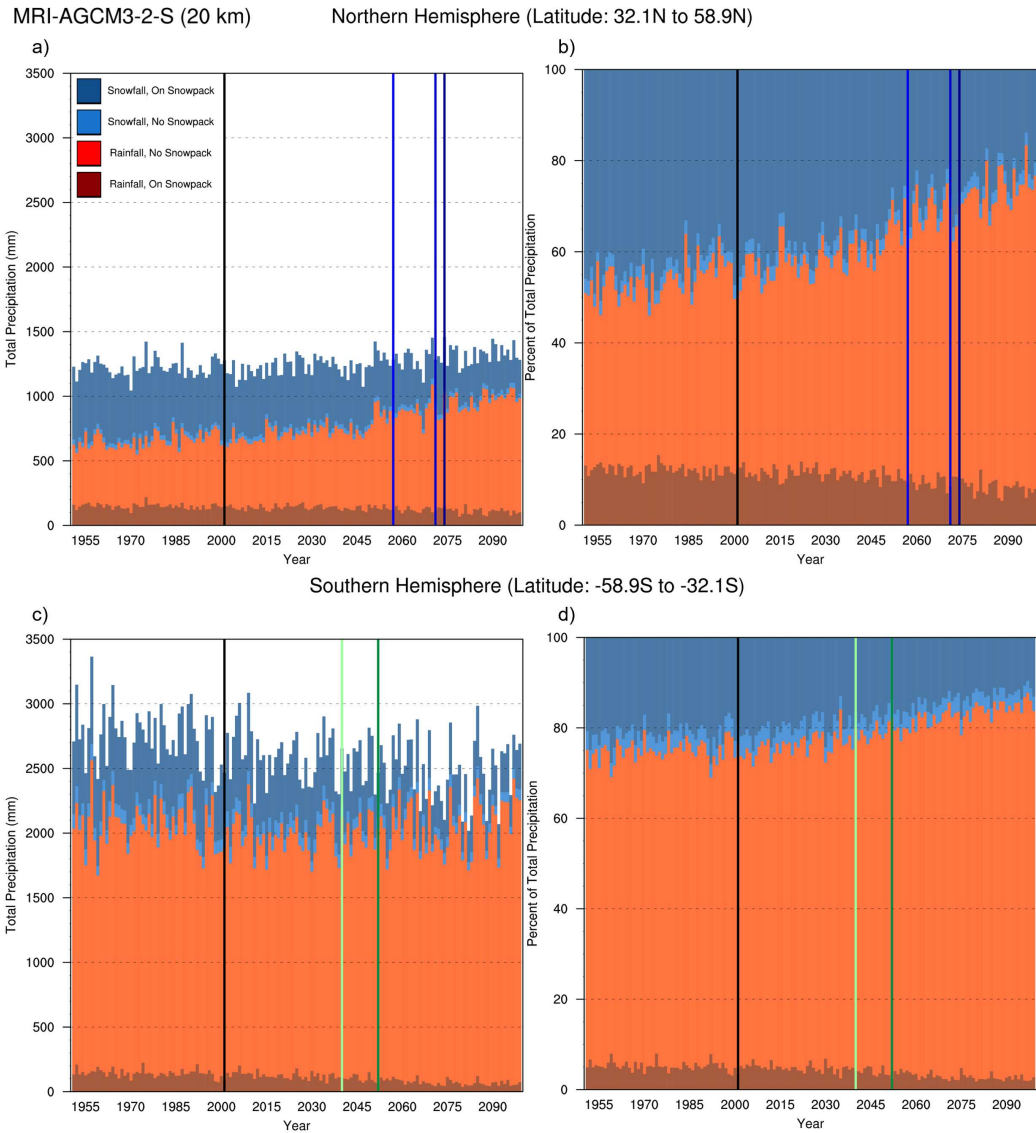


**Figure S12.** Annual mean total precipitation and percentage of annual mean total precipitation associated with rainfall and snowfall with pre-existing snow cover on the surface for the Intermountain West (a, b) and Chilean Andes (c, d) portions of the American Cordillera. The historical reference period end date is shown via a vertical black line and the median date-of-emergence of low-to-no snow for extreme (at least, 2-years), episodic (at least, 5-years), and persistent (at least, 10-years) conditions are also shown with line colors chosen to match with those used in Figure 2. Note that for the Southern Hemisphere the vertical lines indicating the median date-of-emergence for episodic and persistent low-to-no snow are overlapping.

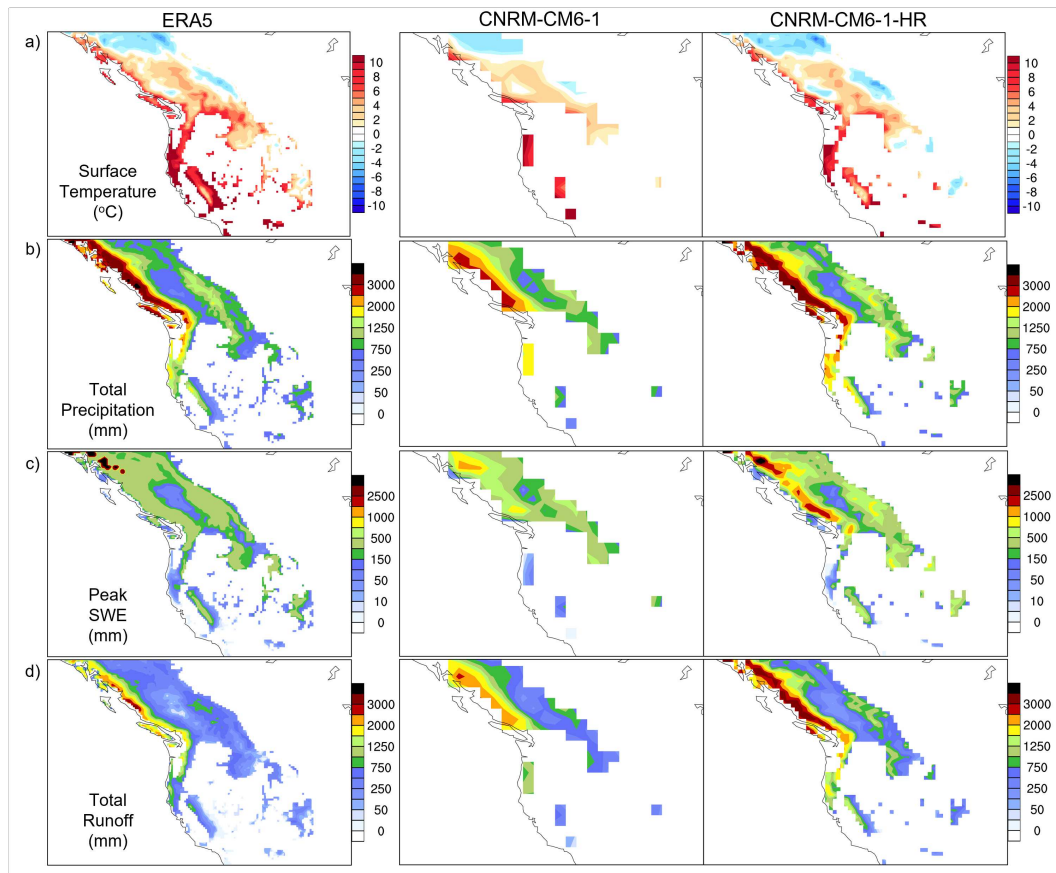


**Figure S13.** CNRM-CM6-1 (~250 km resolution, center) and CNRM-CM6-1-HR (~50 km resolution, far right) 1979-2014 climatological means for the Intermountain West portion (32° N to 59° N) of the American Cordillera. The ECMWF Reanalysis version 5 (ERA5, ~25 km resolution) is shown on the far-left column. Row a) annual mean surface air temperature. Row b) annual mean total precipitation. Row c) annual mean peak SWE. Row d) annual mean total runoff.

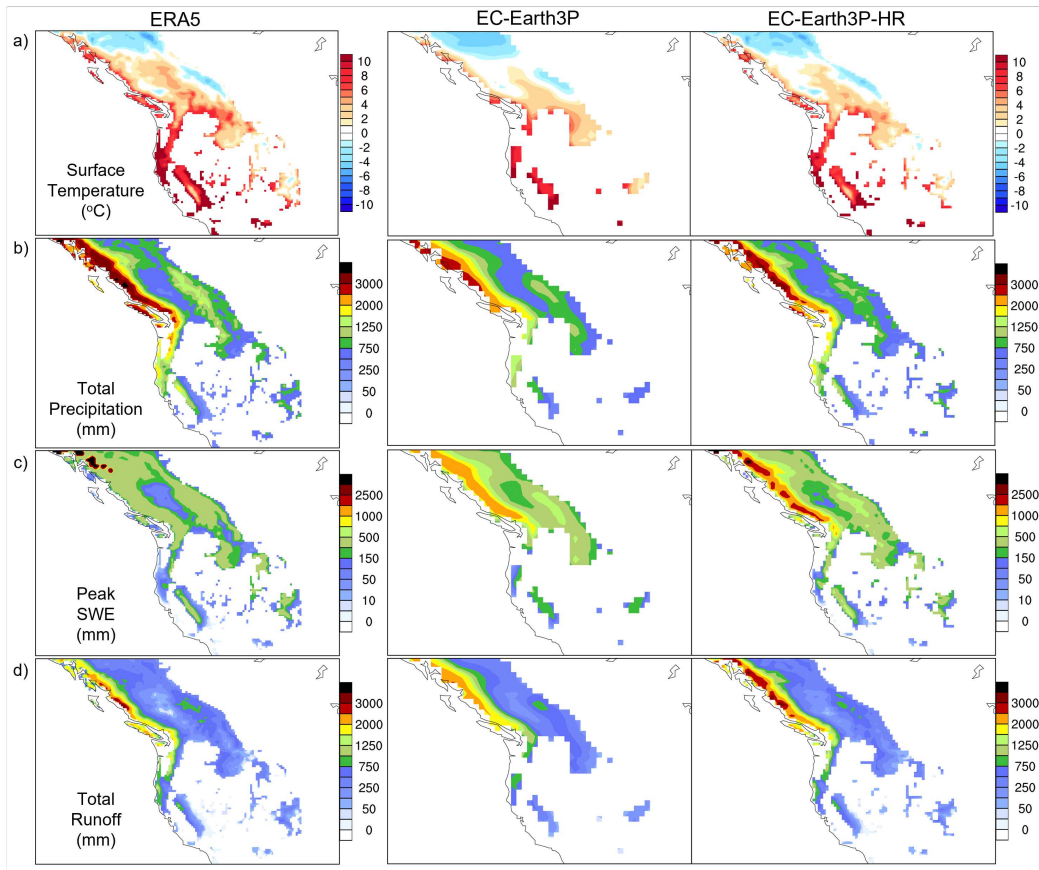


**Figure S14.** EC-Earth3P (~100 km resolution, center) and EC-Earth3P-HR (~50 km resolution, far right) 1979-2014 climatological means for the Intermountain West portion (32° N to 59° N) of the American Cordillera. The ECMWF Reanalysis version 5 (ERA5, ~25 km resolution) is shown on the far-left column. Row a) annual mean surface air temperature. Row b) annual mean total precipitation. Row c) annual mean peak SWE. Row d) annual mean total runoff.

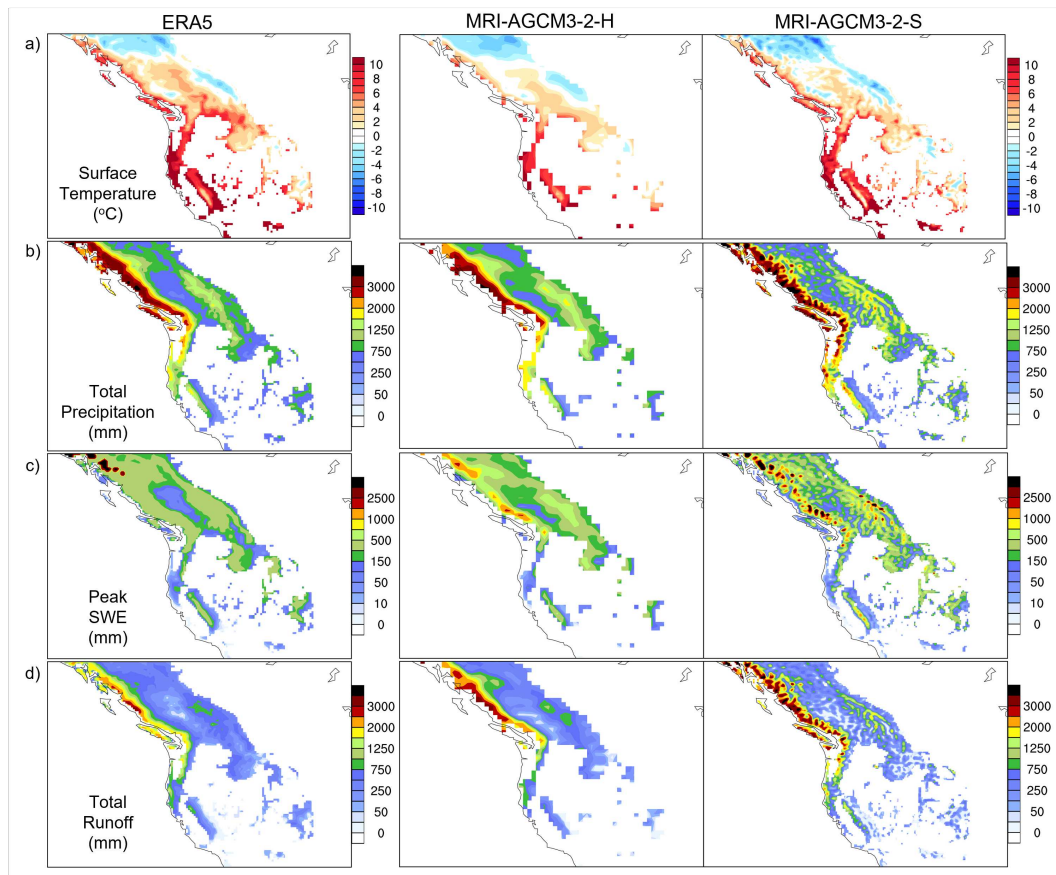


**Figure S15.** MRI-AGCM3-2-H (~60 km resolution, center) and MRI-AGCM3-2-S (~20 km resolution, far right) 1979-2014 climatological means for the Intermountain West portion (32° N to 59° N) of the American Cordillera. The ECMWF Reanalysis version 5 (ERA5, ~25 km resolution) is shown on the far-left column. Row a) annual mean surface air temperature. Row b) annual mean total precipitation. Row c) annual mean peak SWE. Row d) annual mean total runoff.

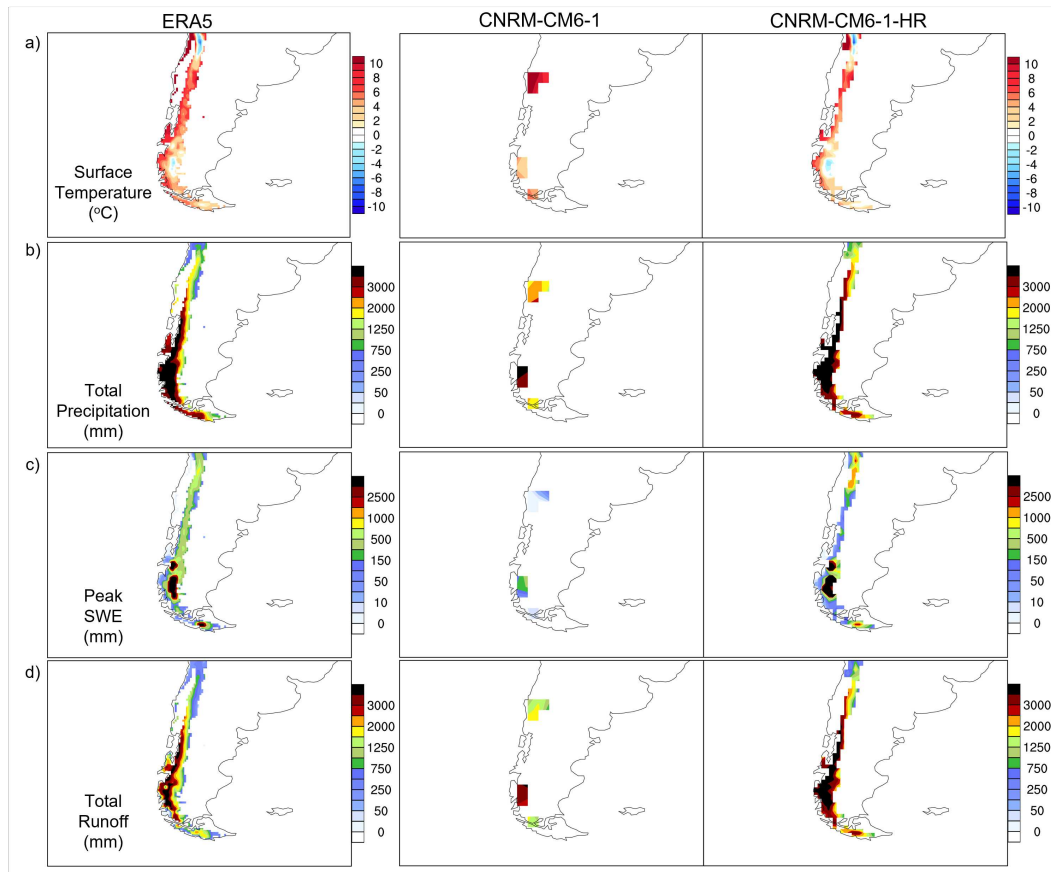


**Figure S16.** CNRM-CM6-1 (~250 km resolution, center) and CNRM-CM6-1-HR (~50 km resolution, far right) 1979-2014 climatological means for the Chilean Andes portion (32° S to 59° S) of the American Cordillera. The ECMWF Reanalysis version 5 (ERA5, ~25 km resolution) is shown on the far-left column. Row a) annual mean surface air temperature. Row b) annual mean total precipitation. Row c) annual mean peak SWE. Row d) annual mean total runoff.

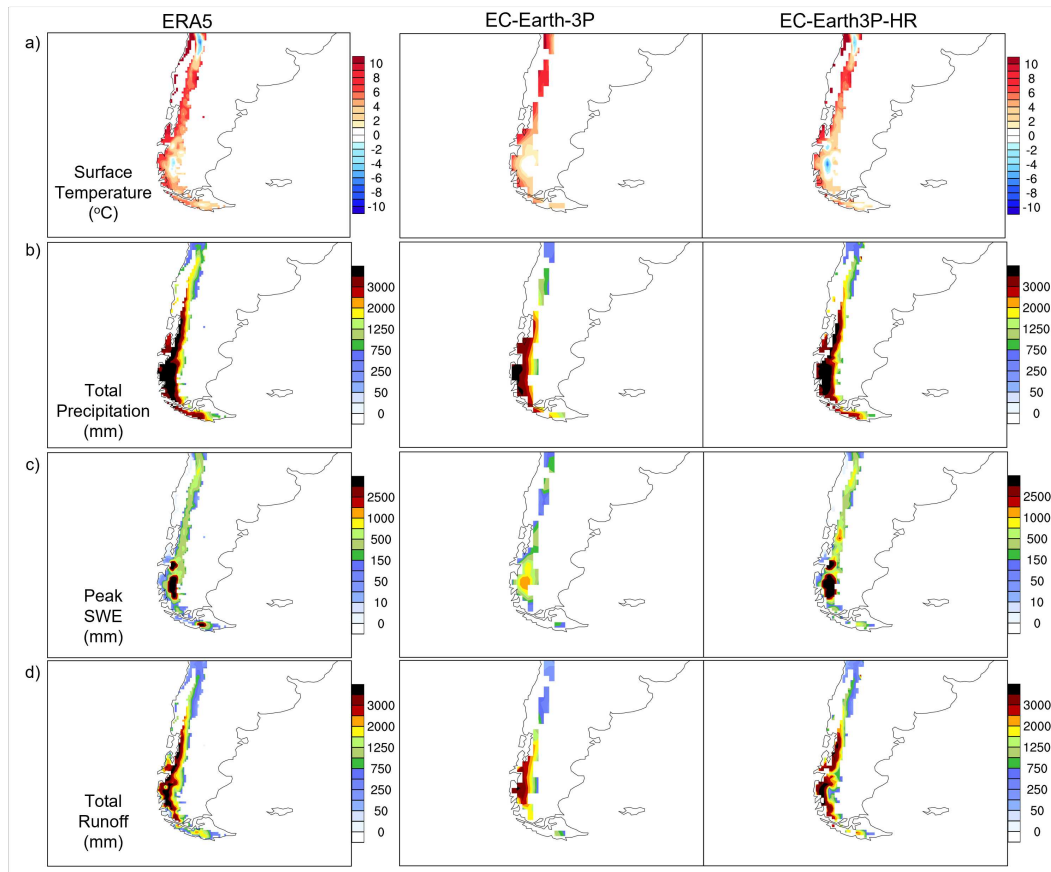


**Figure S17.** EC-Earth3P (~100 km resolution, center) and EC-Earth3P-HR (~50 km resolution, far right) 1979-2014 climatological means for the Chilean Andes portion (32° S to 59° S) of the American Cordillera. The ECMWF Reanalysis version 5 (ERA5, ~25 km resolution) is shown on the far-left column. Row a) annual mean surface air temperature. Row b) annual mean total precipitation. Row c) annual mean peak SWE. Row d) annual mean total runoff.

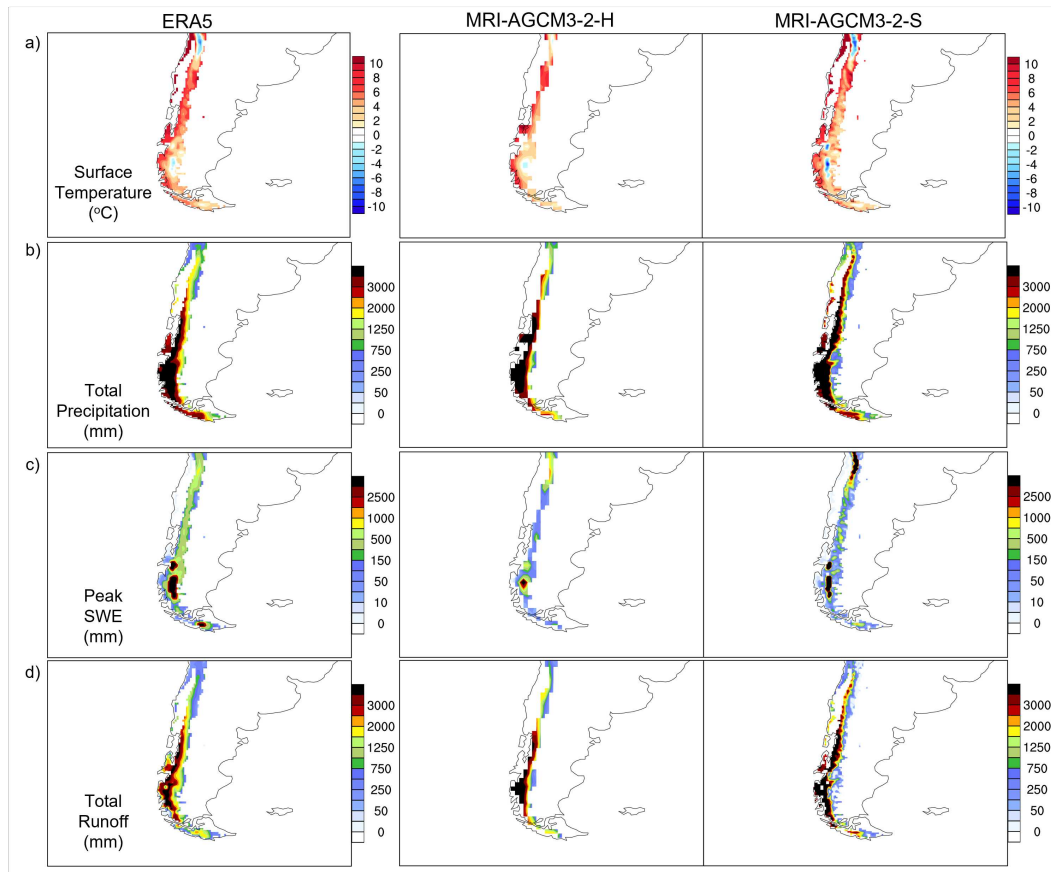


**Figure S18.** MRI-AGCM3-2-H (~60 km resolution, center) and MRI-AGCM3-2-S (~20 km resolution, far right) 1979-2014 climatological means for the Chilean Andes portion (32° S to 59° S) of the American Cordillera. The ECMWF Reanalysis version 5 (ERA5, ~25 km resolution) is shown on the far-left column. Row a) annual mean surface air temperature. Row b) annual mean total precipitation. Row c) annual mean peak SWE. Row d) annual mean total runoff.